Identification of two vibration regimes of underwater fibre optic cables by Distributed Acoustic Sensing

Daniel Mata Flores[1], E. Diego Mercerat[2], Jean-Paul Ampuero[1], Diane Rivet[1], and Anthony Sladen[1]

[1]Université Côte d'Azur
[2]CEREMA

December 7, 2022

Abstract

Distributed Acoustic Sensing (DAS) enables data acquisition for underwater Earth Science with unprecedented spatial resolution. Submarine fibre optic cables traverse sea bottom features that can lead to suspended or decoupled cable portions, and are exposed to the ocean dynamics and to high rates of marine erosion or sediment deposition, which may induce temporal variations of the cable's mechanical coupling to the ocean floor. Although these spatio-temporal fluctuations of the mechanical coupling affect the quality of the data recorded by DAS, and determine whether a cable section is useful or not for geophysical purposes, the detection of unsuitable cable portions has not been investigated in detail. Here, we report on DAS observations of two distinct vibration regimes of seafloor fibre optic cables: a high-frequency (> 2 Hz) regime we associate to cable segments pinned between seafloor features, and a low-frequency (< 1 Hz) regime we associate to suspended cable sections. While the low-frequency oscillations are driven by deep ocean currents, the high-frequency oscillations are triggered by the passage of earthquake seismic waves. Using Proper Orthogonal Decomposition, we demonstrate that high-frequency oscillations excite normal modes comparable to those of a finite 1D wave propagation structure. We further identify trapped waves propagating along cable portions featuring high-frequency oscillations. Their wave speed is consistent with that of longitudinal waves propagating across the steel armouring of the cable. The DAS data on cable sections featuring such cable waves are dominated by highly monochromatic noise. Our results suggest that the spatio-temporal evolution of the mechanical coupling between fibre optic cables exposed to the ocean dynamics and the seafloor can be monitored through the combined analysis of the two vibration regimes presented here, which provides a DAS-based method to identify underwater cable sections unsuitable for the analysis of seismic waves.

Identification of two vibration regimes of underwater fibre optic cables by Distributed Acoustic Sensing

D. Mata Flores[1], E. D. Mercerat[2], J.P. Ampuero[1], D. Rivet[1] and A. Sladen[1]

[1] *Université Côte d'Azur, CNRS, Observatoire de la Côte d'Azur, IRD, Géoazur, Sophia Antipolis,*

250 *Rue Albert Einstein,* 06560, *Valbonne, France*

[2] *CEREMA, Méditerranée,* 500 *Rte des Lucioles,* 06560, *Valbonne, France*

Abstract

Distributed Acoustic Sensing (DAS) enables data acquisition for underwater Earth Science with unprecedented spatial resolution. Submarine fibre optic cables traverse sea bottom features that can lead to suspended or decoupled cable portions, and are exposed to the ocean dynamics and to high rates of marine erosion or sediment deposition, which may induce temporal variations of the cable's mechanical coupling to the ocean floor. Although these spatio-temporal fluctuations of the mechanical coupling affect the quality of the data recorded by DAS, and determine whether a cable section is useful or not for geophysical purposes, the detection of unsuitable cable portions has not been investigated in detail. Here, we report on DAS observations of two distinct vibration regimes of seafloor fibre optic cables: a high-frequency (> 2 Hz) regime we associate to cable segments pinned between seafloor features, and a low-frequency (< 1 Hz) regime we associate to suspended cable sections. While the low-frequency oscillations are driven by deep ocean currents, the high-frequency oscillations are triggered by the passage of earthquake seismic waves. Using Proper Orthogonal Decomposition, we demonstrate that high-frequency oscillations excite normal modes comparable to those of a finite 1D wave propagation structure. We further identify trapped waves propagating along cable portions featuring high-frequency oscillations. Their wave speed is consistent

with that of longitudinal waves propagating across the steel armouring of the cable. The DAS data on cable sections featuring such cable waves are dominated by highly monochromatic noise. Our results suggest that the spatio-temporal evolution of the mechanical coupling between fibre optic cables exposed to the ocean dynamics and the seafloor can be monitored through the combined analysis of the two vibration regimes presented here, which provides a DAS-based method to identify underwater cable sections unsuitable for the analysis of seismic waves.

1 INTRODUCTION

Distributed Acoustic Sensing (DAS) is a revolutionary technology that transforms ordinary telecommunication fibre cables into dense high-resolution strainmeter arrays. Relying on the principles of φ-OTDR (phase-Optical Time Domain Reflectometry), DAS probes fibre optic cables through an interrogator unit that sends a pulsed coherent laser signal and records the Rayleigh backscattered light (Hartog 2017). Measurements of longitudinal strain or strain rate are derived from the phase difference of the light traveling back to the interrogator, using the speed of light and refractive index of the fibre (Hartog 2017). The strain (or strain rate) is averaged over a predetermined cable span whose length is known as the gauge length. DAS channels have a spacing of a few meters across tens of kilometers, providing dense arrays of sensors for several applications, such as on-land/offshore seismology or physical oceanography, at low relative cost with a spatial resolution unreachable by the current instrumentation (Mateeva et al. 2014; Lindsey et al. 2017; Martin et al. 2018; Zhan 2020).

Underwater DAS relies on fibre optic cables traversing different seafloor features, which conditions the quality of the recorded signals. Commonly, underwater fibre cables are designed to connect an on-land facility with either deep ocean instruments or another coastal facility. Cables often cross several bathymetry features from the coast to the abyssal plain, including steep fluctuations of the continental slope and deep valleys on the seafloor. To decrease the deployment cost, offshore cables are often buried only on the first kilometers near the coast. Hence, most of the cables are exposed to the ocean dynamics and the irregularities of the bathymetry, which may lead to cable segments mechanically decoupled from the seafloor or even cable sections hanging in the water column (Mata Flores et al. 2022). A significant correlation between irregular bathymetry and unfavorable DAS measurements has been noted by Lior et al. (2021), for seismology applications of seafloor DAS. They concluded that bathymetry dictates the quality of DAS recordings. It has been also reported that the variation of the mechanical cable/seafloor coupling across long underwater fibre optic cables

has an impact on the amplitude of the strain rate and the type of seismic waves recorded by DAS (Lindsey et al. 2019; Sladen et al. 2019; Williams et al. 2019).

The mechanical coupling between the cable and the seafloor is expected to fluctuate along underwater fibre optic cables. Although this variation determines whether a cable section is useful or not for DAS applications in seismology, the detection of unsuitable cable portions through DAS has not been previously addressed. Maintenance works of seafloor fibre optic cables usually supply real-time images of the cable conditions. However, the cost of these direct inspections is commonly high and increases with the type of remotely operated underwater vehicle (ROV) surveying the cable. Moreover, ROV inspections are not regularly scheduled, which prevents monitoring the temporal evolution of the mechanical cable/seafloor coupling. This situation calls for generic approaches based on fibre sensing techniques capable of continuous monitoring, considering that seafloor fibre optic cables are exposed to ocean dynamics or areas with high rates of marine erosion/sediment deposition. A method identifying underwater cable sections featuring unfavorable coupling with the sea bottom is then crucial to harness offshore DAS for seismology applications. We report here observations of two vibration regimes recorded by DAS across seafloor fibre optic cables: high-frequency and low-frequency oscillations. We associate the former with cable segments pinned at their ends by seafloor features and the latter with suspended cable sections.

In this study, we identify seismic waves exciting high-frequency oscillations of three seafloor fibre optic cables located in the Mediterranean sea. We extract normal modes of these oscillations by Proper Orthogonal Decomposition and we compare them with those of a 1D wave propagation model. We further calculate the speed of trapped waves propagating along the cable portions featuring the oscillations. Then, we compare the high-frequency oscillations to low-frequency oscillations detected along presumably hanging cable segments. Our results suggest that the spatio-temporal evolution of the mechanical coupling between fibre cables exposed to the ocean dynamics and the seafloor can be monitored through the two vibration regimes presented here.

This article is organized as follows. In the next section, the DAS recordings and their main characteristics are described. Then, in Section 3, the high-frequency oscillations are analyzed, their normal modes are extracted and the cable waves generated during the vibrations are studied. In Section 4, the high-frequency oscillations are compared to the low-frequency oscillations. Finally, we discuss the implications of the two vibration regimes on the mechanical cable/sea bottom coupling and on the type of seismic waves recorded by DAS.

2 DATA OVERVIEW

This study uses DAS data acquired in the Mediterranean sea along three underwater electro-optic fibre cables: one located in Toulon, south of France, and two situated offshore Methoni, southwest Greece. The three cables were deployed to power and retrieve data from instruments installed at their offshore ends (Coyle 2017; Aggouras et al. 2005; Anassontzis and Koske 2003). The cable trajectories and bathymetry profiles presented here are estimated using the cable deployment coordinates and bathymetry maps taken from the EMODnet (European Marine Observation and Data Network) platform, with a cell size of ∼111 m. Due to oceanography processes, such as deep-sea currents, or bathymetry irregularities, the real cable locations may differ from the ones adopted here. We provide more details on the cables and associated DAS measurement campaigns below.

2.1 DAS experiment on the HCMR and NESTOR cables

DAS strain rate data were acquired along the contiguous HCMR (Hellenic Center for Marine Research) and NESTOR (Neutrino Extended Submarine Telescope with Oceanographic Research) fibre optic cables (Figure 1), located offshore Methoni at the deepest part of the Mediterranean in Greece, southwest of the Peloponnese (Collaboration et al. 1994; Anassontzis et al. 1998; Aggouras et al. 2005). The HCMR cable communicates an on-land facility with an oceanography laboratory. The cable is 13.2 km long and includes 12 single-mode fibres protected by a Single Armouring (SA) of galvanized steel wires. The NESTOR cable was deployed for data transmission of a deep sea neutrino telescope, but it was abandoned after several failures on the cable. It is composed of 18 single-mode fibres that are protected by a Heavy Armouring (HV) made of two layers of galvanized steel wires along the first 12.5 km, and from there to its terminal point at 26.2 km by a Light Armouring (LA) made of one layer of galvanized steel wires. Both cables are buried for the first 2 km inside the Methoni Bay, following parallel paths, at a depth ranging from 0.5 to 1.5 m below the seabed. Outside the bay, the cables lay on the seafloor following different directions. The HCMR cable mostly points to the West, reaching a depth of 1530 m. The NESTOR cable points to the South-West and reaches a depth of 3820 m (Lior et al. 2021).

The HCMR and NESTOR cables were sensed in 2019, between 18-April 16:20:22 UTC and 25-April 04:30:15 UTC, by a Febus Optics A1-R DAS interrogator unit. The former was interrogated on the first 48 h of the experiment, and the latter during the rest of the DAS campaign. The A1-R DAS unit interrogates the fibre using a single-pulse phase-based system that generates strain rate recordings. Longitudinal cable strains are obtained by the optical
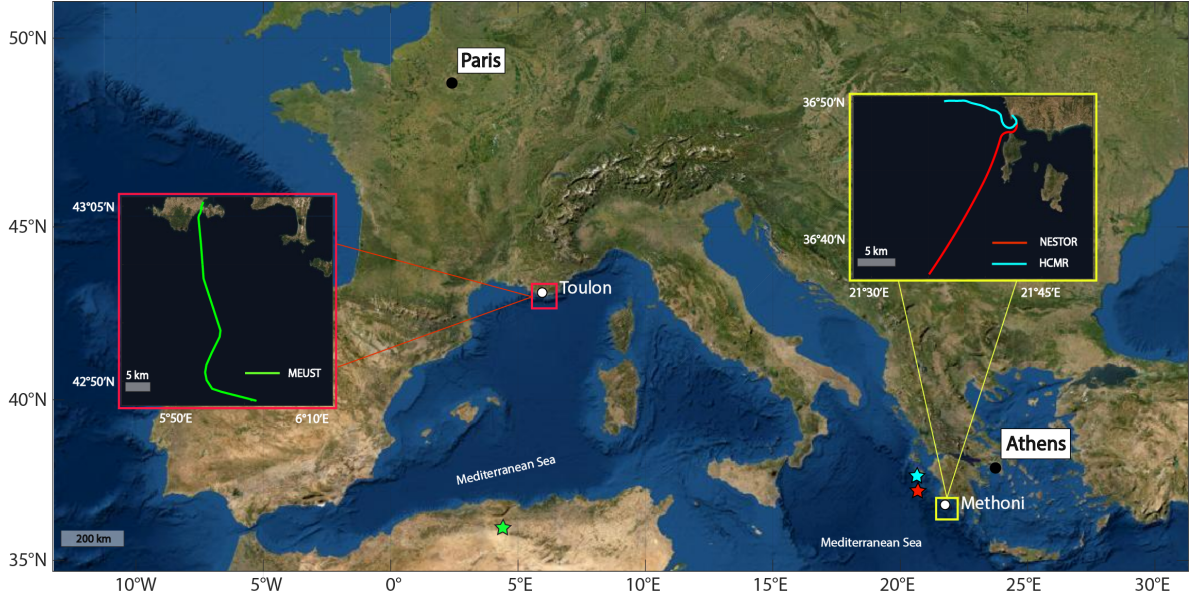
Figure 1. Location of the underwater HCMR, NESTOR and MEUST electro-optic fibre cables. (yellow rectangle) The 13.2-km-long Hellenic Center for Marine Research (HCMR) and the 26.2-km-long Neutrino Extended Submarine Telescope with Oceanographic Research (NESTOR) fibre cables, situated offshore Methoni Bay, Greece. DAS data were acquired in HCMR and NESTOR cables between 18-April-2019 16:20:22 UTC and 25-April-2019 04:30:15 UTC. (cyan and red stars) Epicenters of: a M_L-3.7 earthquake recorded along HCMR cable, origin time 18-April-2019 21:44:42 UTC, and a M_L-3.3 earthquake recorded along NESTOR cable, origin time 22-April-2019 19:26:06 UTC, respectively (Lior et al. 2021). (red rectangle) The 44.8-km-long Mediterranean Eurocentre for Underwater Sciences and Technologies (MEUST) fibre cable, located offshore Toulon, France. A DAS experiment was conducted along the MEUST cable between 11-July-2019 13:12:16 UTC and 31-July-2019 08:19:26 UTC. (green star) Epicenter of a M_L-3.9 earthquake recorded along the MEUST cable, origin time 22-July-2019 16:23:07 Local Time.

dephasing between two points along the fibre cable, at a specified gauge length distance. We set the DAS interrogator to acquire with a pulse width of 5 m, a spatial resolution of 3.2 m, and pulse rate frequencies of 500 Hz on the HCMR cable, and 1400 and 1000 Hz for the first and last 4 days on the NESTOR cable, respectively. The gauge length was set to 19.2 m for both cables, generating an array of 688 and 1365 equally-spaced sensors along the HCMR and NESTOR cables, respectively.

Two earthquakes recorded by DAS along the HCMR and NESTOR cables are used in this study. A M_L-3.7 earthquake (epicenter, cyan star in Figure 1) identified by the EMSC (European Mediterranean Seismological Centre), with origin time 18-April-2019 21:44:42 UTC, was clearly observed in the DAS-data recorded along the HCMR cable. Similarly, a M_L-3.3

earthquake was recorded across the NESTOR cable (epicenter, red star in Figure 1). This earthquake was cataloged by the Athens University, with origin time 22-April-2019 19:26:06 UTC.

2.2 DAS experiment in Toulon, France

DAS strain data were collected along the MEUST (Mediterranean Eurocentre for Underwater Sciences and Technologies) optic fibre cable, situated offshore Toulon, south of France (Figure 1). The cable bridges landward a multi-physics-and-communication station and the KM3NeT/ORCA (Oscillation Research with Cosmics in the Abyss) neutrino detector located at the cable underwater termination point, as part of the MEUST-NUMerEnv (NeUtrino Mer Environment) project (Lamare 2016; Coyle 2017). The MEUST cable spans 44.8 km and its armouring progressively changes oceanward, as follows: a Double Armouring (DA) of two layers of galvanized steel wires along the first 2.1 km offshore, then a Single Armouring (SA) of one layer of galvanized steel wires for the next 15.1 km, and finally a metallic screen until the cable termination point. Only the first 500 m of cable are buried offshore. Afterward, the cable lays on the seafloor and traverses different oceanic features until reaching a maximum depth of 2420 m.

The MEUST cable was sensed combining a DAS-interrogator from Aragon Photonics (HDAS) with Raman amplification. Distributed Raman amplification guarantees longitudinal (along the cable axis) strain recordings with an instrumental noise floor variation of < 5 dB (Fernández-Ruiz et al. 2019; Williams et al. 2019; Pastor-Graells et al. 2016; Lior et al. 2021). The instrumental noise floor was observed to be below 100 $picostrain/\sqrt{Hz}$ along the cable, which is comparable to optimal laboratory measurements for long fibres (Fernández-Ruiz et al. 2019; Lior et al. 2021). During the DAS experiment performed between 11-July-2019 13:12:16 UTC and 31-July-2019 08:19:25 UTC, the pulse wavelength was set to 1550 nm, with 100 ns width (equivalent to a spatial resolution of 10 m), 1 GHz spectral content and 50 mW peak power. Corning© LEAF (Large Effective Area Fiber) optic fibres featuring a light attenuation (<0.19 dB/km) are integrated in the MEUST cable, which also improved the detection range. The longitudinal strain was sampled at a rate of 100 Hz during the first 10 days of the experiment and 500 Hz in the remaining part of the campaign. The gauge length was set at 10 m, creating a network of 4480 equally-spaced strain sensors across the cable. To prevent low-frequency noise affecting the strain recorded by DAS, as suggested by R. Fernández-Ruiz et al. (2019), we converted the strain data to strain rate by computing its

finite-difference time derivative. The data set used here is composed of strain rate recordings comparable to the ones collected during the Greek experiment.

A M_L-3.9 earthquake recorded by DAS along the MEUST cable is used in this study. The epicenter of the earthquake (green star in Figure 1) was identified by the IGN ("*Instituto Geográfico Nacional*", Spanish for "*National Geographic Institute*") at northern Algeria, with origin time 22-July-2019 16:23:07 Local Time.

3 FIBRE OPTIC CABLE OSCILLATIONS TRIGGERED BY EARTHQUAKES

3.1 Detection of high-frequency oscillations

DAS recordings show that the passage of earthquake seismic waves along underwater fibre optic cables excites high-frequency oscillations that remain trapped within certain cable sections. We analyze the strain rate recorded by DAS along the NESTOR, HCMR and MEUST cables, at the time of the three earthquakes aforementioned, low-pass filtered with a cutoff frequency of 20 Hz. Oscillations with frequencies above 2 Hz appear simultaneously in cable portions with different span lengths, at the same time as the passage of seismic waves, as shown in Fig.2(c) for the NESTOR cable. We refer to these oscillations as "*high-frequency oscillations*" or HF oscillations. Figure 2 shows an example during a M_L-3.3 earthquake recorded by DAS in the NESTOR cable (Figure 2.a). HF oscillations are confined within some cable segments. We select a 1-min window, 40 s after the origin time of the earthquake, in which HF oscillations are visible, and calculate the Fourier spectrum for each channel. The spectra show fundamental and harmonic frequencies excited above 2 Hz (Figure 2.c). HF oscillations are not visible on 1-min windows 90 s before and 180 s after the origin time of the earthquake. In contrast, signals with frequency lower than 1 Hz exist at all times on certain cable segments (Figure 2.b,d): these low-frequency oscillations are related to a different process discussed later on. A similar behavior is observed for earthquakes recorded along the HCMR and MEUST cables (*Supplementary Figures S1 and S2*).

The relation between the frequencies of HF oscillations and the span lengths of the cable portions that host them suggests they are made of waves trapped along the cable. We measure the fundamental frequencies of the HF oscillations excited by the three earthquakes, and plot them as a function of the span length L of their hosting cable segment (Figure 3). We find that they follow the equation:

$$f_n = \frac{nV}{2L} \tag{1}$$
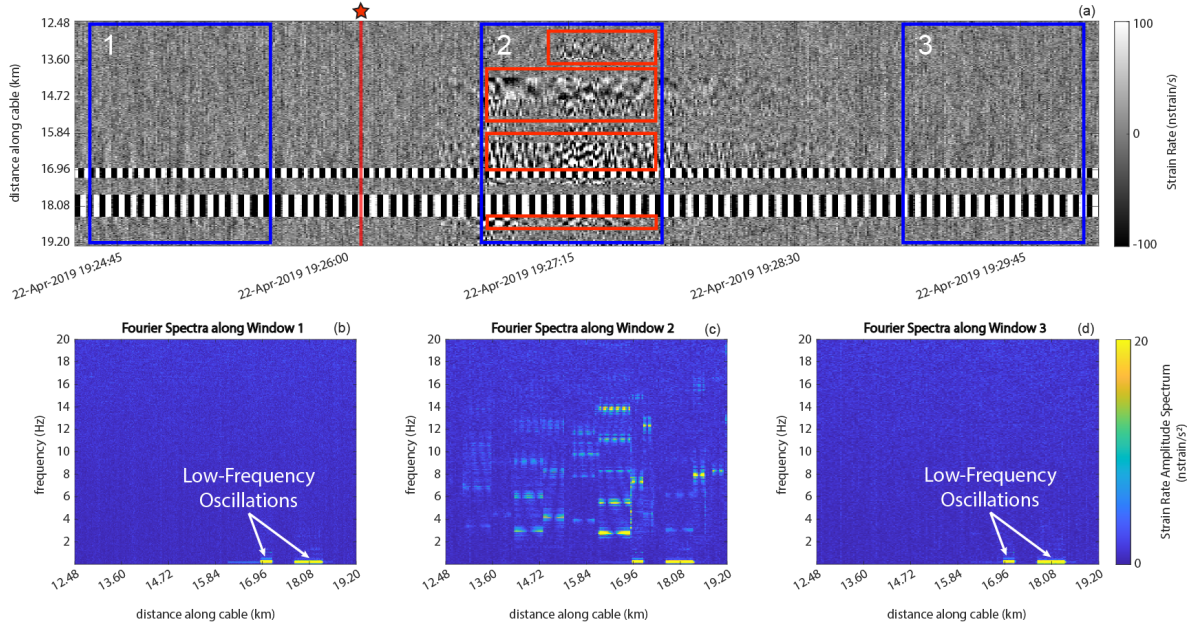
Figure 2. High-frequency vibrations triggered along the NESTOR fibre cable after a M_L-3.3 earthquake is recorded by DAS. (a) Low-pass filtered strain rate between km 12.48 and 19.20 along the NESTOR cable, from 22-April-2019 19:24:45 to 19:30:15 UTC. Strain rate is filtered below 20 Hz. (red star) Origin time of the M_L-3.3 earthquake of Fig. 1 is indicated as reference (Lior et al. 2021). (red rectangles) Waves trapped along certain cable sections can be observed after the arrival of seismic waves. (b), (c) and (d) Fourier Spectra between km 12.48 and 19.20 of a 1-min window starting: 90 s before the earthquake (1), 40 s after the earthquake (2) and 180 s after the earthquake (3), respectively. Fourier spectra before (b) and after (d) the earthquake are dominated by excited frequencies lower than 1 Hz. Fundamental-and-harmonic frequencies higher than 2 Hz appear after the arrival of seismic waves along different cable spans (c), from km 12.48 to 19.20.

that describes the frequency f_n of the n-th normal mode of wave propagation in a 1D elastic medium with fixed ends, wave speed V and length L (Thompson et al. 1975; Yigit and Choura 1995). Fundamental frequencies ($n = 1$) recorded along different segments of the MEUST, HCMR and NESTOR cables are consistent with a wave speed $V = 4000$ m/s $\pm$ 400 m/s (Figure 3). Similarly, the first and second harmonics ($n = 2, 3$) in the NESTOR cable are in agreement with eq. (1) and the same wave speed (Figure 3). The implications of the wave speed value obtained are described in section 3.3.

3.2 Normal modes of the high-frequency oscillations

Modal analysis further supports that the propagation of longitudinal waves along a vibrating string is one of the simplest models to explain the HF oscillations. Modal analysis is commonly
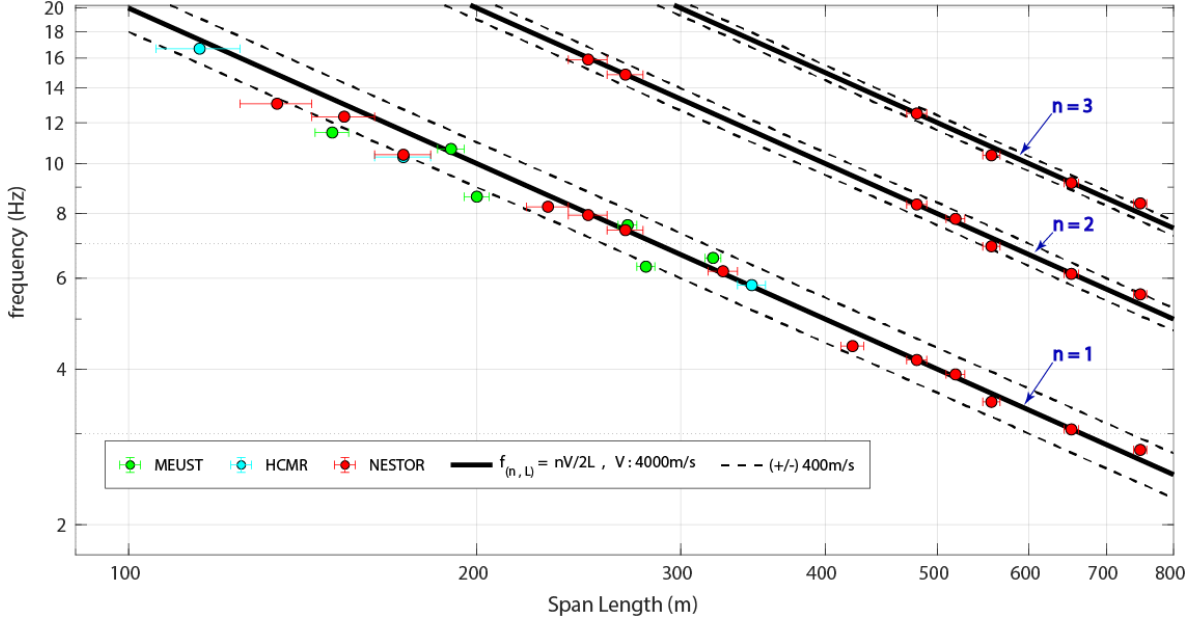
Figure 3. Natural frequencies of earthquake-triggered oscillations as a function of underwater fibre cable spans. Natural frequencies recorded by DAS during EQ-triggered fibre cable oscillations are represented as a function of the cable span length featuring the vibration for the MEUST (green), NESTOR (red) and HCMR (cyan) cables. Error bars indicate half of the gauge length used during each DAS experiment. The black continuous lines follow the equation $f_n = nV/2L$ of the n-th natural frequency f_n of a 1D elastic medium with fixed ends, wave speed V and length L. Values of $n = 1, 2, 3$ represent the fundamental mode, the first and the second harmonic, respectively. A wave speed $V = 4000$ m/s (solid lines) with a deviation of $\pm$ 10% (dashed lines) is consistent with the natural frequencies of MEUST, HCMR and NESTOR cables.

used to characterize the normal modes of a vibrating structure, and the Proper Orthogonal Decomposition (POD) is a popular technique for examining modal activity (Feeny 2002). The POD method, also known as Karhunen-Loève decomposition, is a statistical approach to obtain optimal distributions of energy from a set of recordings (Feeny 2002). It has been widely used to generate empirical modes for modal reduction of nonlinear systems (Kappagantu and Feeny 1999, 2000), to yield a measure of spatial coherence (Cusumano and Bai 1993; Cusumano et al. 1993), and for modal analysis (Feeny and Kappagantu 1998). POD results in a family of proper orthogonal modes (POMs) that are extracted from the correlation matrix of a set of time series (Feeny 2002). We extract normal modes from 1-min windows of the HF oscillations described in 3.1, using POD. The correlation matrix used for the POD calculations is composed of the strain rate recorded by DAS along the cable segments featuring HF oscillations.

We compare normal modes extracted by POD from HF oscillations to those of a 1D wave

propagation structure with fixed ends. The normal modes (Φ_n) of a vibrating string fixed at its ends are described by:
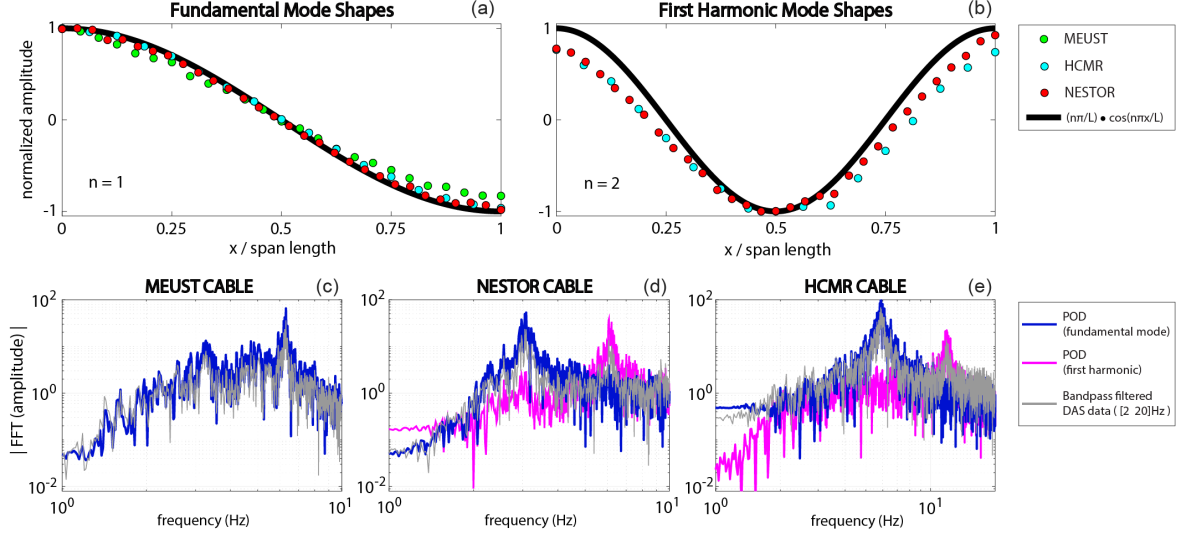
$$\Phi_n(x) = \sin\left(\frac{n\pi x}{L}\right) \tag{2}$$

with n and L as defined for eq. (1), and $x \in [0, L]$ the relative location along the span length (Yigit and Choura 1995). We calculate the spatial derivative $\partial\Phi_n(x)/\partial x$ of eq. (2), which provides the modes expected for strain rate data. The fundamental mode derived from the cable vibrations by POD has the same shape as the theoretically expected fundamental mode (Figure 4.a), regardless of the cable location and the DAS-interrogator used (POMs calculations in the *Supplementary Material*). Similarly, the first harmonic mode extracted from the NESTOR and HCMR cable oscillations by POD is in agreement with the model prediction (Figure 4.b).

Natural frequencies recorded by DAS during HF oscillations are in agreement with the ones extracted by POD. POMs derived from POD can be used as basis functions to define proper orthogonal modal coordinates (POCs). Each time-dependent POC represents the amplitude time series associated to its corresponding POM, and its frequency content provides information of the number of active modes (Feeny 2002). We calculate the Fourier transform of the POCs derived from the POMs of Fig. 4(a), for cable segments of the MEUST, NESTOR and HCMR cables that span 280.00, 652.80 and 345.60 m, respectively. We compare them with the Fourier spectra obtained from vibrating cable spans at relative positions (i.e. distance along span normalized by span length) of 0.125, where the fundamental and first harmonic normal modes should have non-zero amplitude according to Fig. 4(a,b). We observe that the fundamental frequency of the HF oscillations recorded by DAS in the three cables is in agreement with the one extracted by POD (Figure 4.c,d,e). In the case of the NESTOR and HCMR fibre cables, harmonic frequencies were also measured during the cable vibrations. We note that those harmonic frequencies correspond as well to the ones derived from the POCs' spectra.

3.3 Cable waves in underwater fibre optic cables

Cross-correlation analysis of DAS data indicates that the HF oscillations are composed of waves traveling along the cable and trapped within bounded cable spans. We calculate cross-correlation functions between strain rate time series of pairs of DAS channels along cable spans featuring HF oscillations. To avoid high-frequency noise, the strain rate data were band-pass filtered between 2 and 20 Hz. Then, cross-correlations were computed over 60-s-long

Figure 4. Proper Orthogonal Decomposition (POD) of high-frequency fibre cable oscillations compared to Normal Modes of a vibrating string. (a) Spatial derivative $\partial\Phi_n(x)/\partial x$ of the normal modes $\Phi_n(x) = sin(n\pi x/L)$ of a vibrating string (black) compared to the Proper Orthogonal fundamental-Modes extracted from a 1-min-long window of fibre oscillations recorded during an EQ in: MEUST cable between km 18.90 and 19.18 (green), NESTOR cable between km 14.13 and 14.78 (red), and HCMR cable between km 9.69 and 10.04 (cyan). Vertical and horizontal axes are normalized by the maximum amplitude of the Normal Mode derivative and the span length L, respectively. (b) Sames as a, but for the Proper Orthogonal first-harmonic-Mode of NESTOR and HCMR cables. (c, d and e) Fourier spectra of the POD-extracted fundamental and first-harmonic mode time series $|\mathcal{F}(POC(t)_1)|$ and $|\mathcal{F}(POC(t)_2)|$ (blue and magenta, respectively) compared to the Fourier spectra of the 1-min fibre cable oscillations indicated in a and b, band-pass filtered between 2 and 20 Hz (gray). Proper Modes extracted through POD of the fibre strain oscillations recorded by DAS are in agreement with those of a 1D vibrating structure fixed at its ends.

consecutive windows, using as reference trace the first oceanward DAS channel featuring the oscillations. The cross-correlation traces show waves traveling back and forth along segments of all three cables: Figure 5(c,e) shows examples from two sections of the NESTOR cable, while examples for the MEUST and HCMR cables can be found in *Supplementary Figures 3 and 4*. For all three cables, the trapped waves travel at speeds ranging from 3939 to 4080 m/s (Figure 5.c,e, Supplementary Figures 3.c,e and 4.c,e), consistent with the speed obtained in Fig. 3, and close to the compressional speed of stainless steel ~ 5000 m/s (Haynes 2014). This observation is in agreement with the property that longitudinal waves in a composite cable are primarily controlled by the characteristics of the stiffer and denser material, here the steel armouring of the cable (Miller et al. 2018).
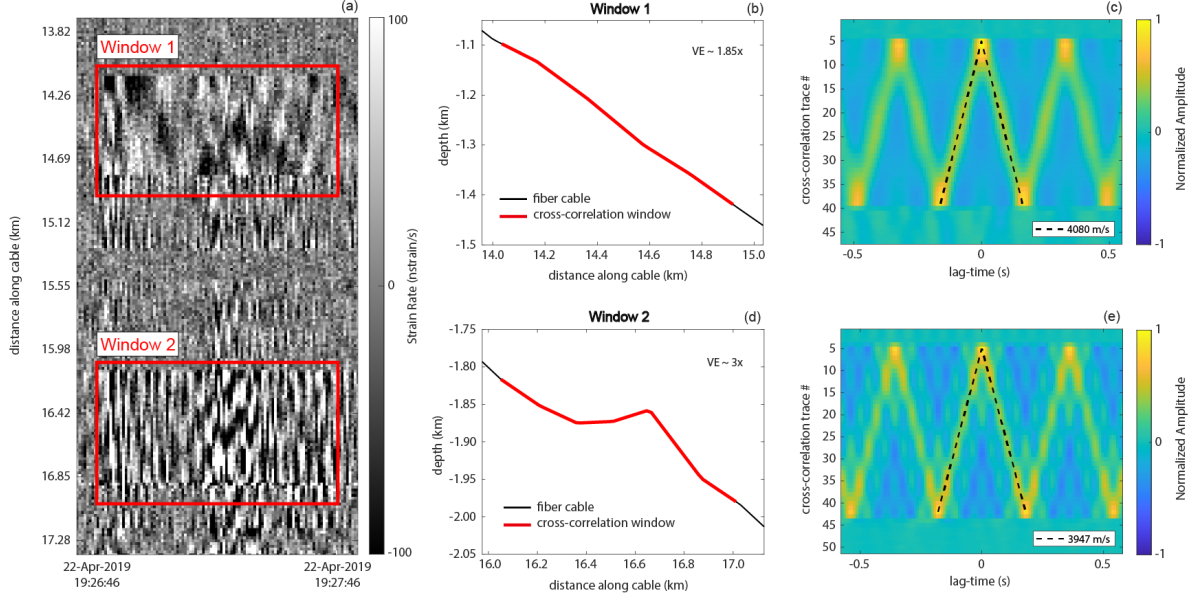
Figure 5. Longitudinal trapped waves detected by DAS along cable segments featuring earthquake-triggered vibrations. (a) Band-pass filtered strain rate between km 13.82 and 17.28 along the NESTOR cable, from 22-April-2019 19:26:46 to 19:27:46 UTC. Strain rate is filtered between 2 and 20 Hz. (red rectangles) Two 60-s-long windows of 883.2 (1) and 960 m (2) width are indicated as reference. (b) Bathymetry profile between km 14 and 15 along the cable path (VE stands for Vertical Exaggeration). The red line highlights the location of window 1 in (a). (c) Cross-correlation traces calculated over window 1 in (a), and relative to the trace reference number 5, km 14.13 along the cable. Amplitudes are normalized by the maximum of the cross-correlation traces. A longitudinal trapped wave bouncing forward and backward along the cable span with a speed of 4080 m/s can be clearly observed (black dashed lines). (d and e) Same as b, and c, but for a cable section presumably suspended between km 16 and 17, window 2 in (a).

The fact that cable waves are trapped indicates that there are changes in the mechanical cable/seafloor coupling along the cable. Local seafloor conditions affect the mechanical coupling between underwater fibre cables and the sea bottom. Indeed, cable sections can be partially or completely buried, just laying on the seafloor, or even hanging (Mata Flores et al. 2022). As previously reported in borehole DAS data, fibre cable segments that are decoupled from the borehole wall can host the propagation of longitudinal vibrations along the cable, the so-called *"cable waves"* detected by Munn et al. (2017). However, to the best of our knowledge, cable waves have not been previously reported in the literature of underwater DAS. Chang and Nakata (2022) observed similar waveforms and wave speeds than the ones we present in Fig 5, for a borehole DAS experiment. They attributed the waveforms to waves likely propagating in the stainless steel cable jacket or the steel well-casing. They also observed similar
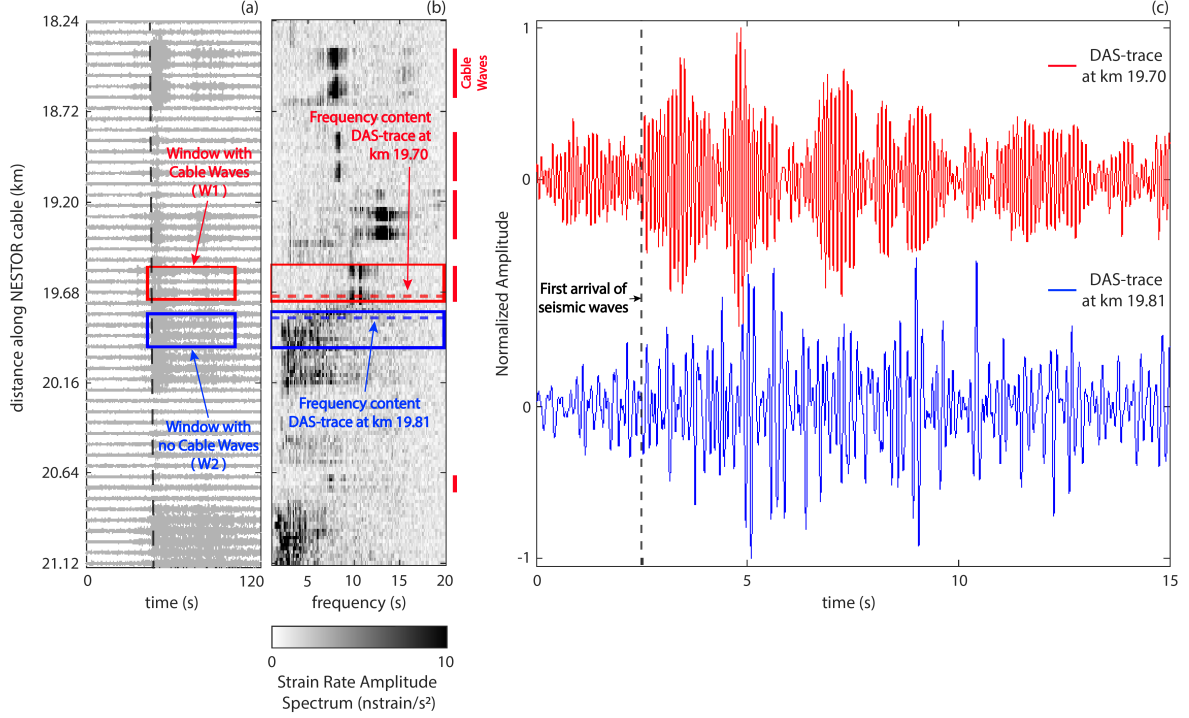
Figure 6. Noise generated by cable waves in DAS-strain rate recordings of the NESTOR cable. (a) 120-s-long traces of band-pass filtered strain rate between km 18.24 and 21.12 along the NESTOR cable. Traces are filtered between 1 and 12 Hz and are represented each 57.6 m. (dashed line) Arrival of seismic waves due to the M_L-3.3 earthquake of Fig. 1. (red and blue rectangles) As reference, 60-s-long windows of 172.8 m width indicate whether cable waves are detected (W1) or absent (W2), respectively. (b) Fourier spectra between km 18.24 and 21.12 of a 60-s-long window starting at the same time of W1 in (a). (red and blue rectangles) Frequency content of W1 and W2, respectively. (c) 15-s-long traces of strain rate along: km 19.70, in W1 (red) and km 19.81, in W2 (blue). Amplitudes are normalized by the maximum strain rate of each DAS-channel. Cable waves are clearly recorded in W1, which may explain the high monochromatic noise that dominates the signal along the DAS-trace in km 19.70, after the arrival of seismic waves, compared to the DAS-trace in km 19.81.

normal mode shapes and natural frequencies for cable or casing waves than those we obtain from the POD of the HF oscillations presented here. We detect the cable waves along cable segments traversing steep continental slopes or deep ocean valleys (Figure 5.b,d, respectively), which may allow cable spans pinned between two points of the sea bottom.

Cable waves generated by earthquakes may reveal cable segments that are unsuitable for DAS applications in seismology. The detection of earthquake-triggered cable oscillations indicates cable spans affected by monochromatic noise due to the generation of cable waves. Figure 6.(c) shows DAS-strain rate recordings across the NESTOR cable, collected during

the arrival of the seismic waves generated by the M_L-3.3 earthquake of Fig. 1. We selected two DAS-channels on the NESTOR cable separated by 110 m (Figure 6.(a,b)): the first at km 19.70 in window W1 containing cable waves and the second at km 19.81 in window W2 without cable waves. Assuming that the variability of the incidence angle and epicentral distance effects of the earthquake are weak at this scale, both DAS-channels should record similar waveforms. Highly monochromatic noise affects the DAS-trace at km 19.70 after the arrival of seismic waves, while the DAS-recordings at km 19.81 are unaffected by this type of noise. We associate the noise in W1 with the propagation of cable waves along this segment. The high-amplitude noise introduced by the cable waves prevents from detecting latter seismic phases across cable sections featuring HF oscillations. Therefore, the detection of cable waves by DAS may help to evaluate the usability of certain cable segments for DAS-applications in underwater seismology.

4   LOW-FREQUENCY OSCILLATIONS COMPARED TO HIGH-FREQUENCY OSCILLATIONS

As mentioned in section 3.1, fibre cable oscillations at frequencies lower than 1 Hz are also detected by DAS. We refer to these oscillations as "*low-frequency oscillations*" (LF oscillations), since their fundamental frequencies are lower than those of the HF oscillations. We observe LF oscillations that extend coherently between pairs of points along the MEUST, NESTOR and HCMR cables. As previously reported by Mata Flores et al. (2022), LF oscillations can last from hours to days and they occur along hanging sections of underwater fibre cables exposed to Vortex-Induced Vibrations (VIV) driven by deep ocean currents. We occasionally observe harmonics of these oscillations (*Supplementary Figure 5*). In this study, we examine the vibration modes and calculate cross-correlations along the cable spans featuring LF oscillations in order to compare the results with the ones already obtained for the HF oscillations.

The LF oscillations show a dominant normal mode shape with quasi-uniform strain rate, a box-car shape. The same normal mode shape is retrieved by POD analysis from the three cables, during periods containing LF oscillations, which we call the "*dominant normal mode*" (Figure 7). The LF dominant normal mode does not correspond with the fundamental mode of strain along a vibrating string, presented in Fig. 4(a), since it does not feature nodes along the cable span. Spectral analysis of the POC derived from the dominant normal mode shows a dominant frequency, which corresponds with the one recorded by DAS during the LF oscillations.

Key aspects of the box-car shape featured by dominant normal modes can be interpreted
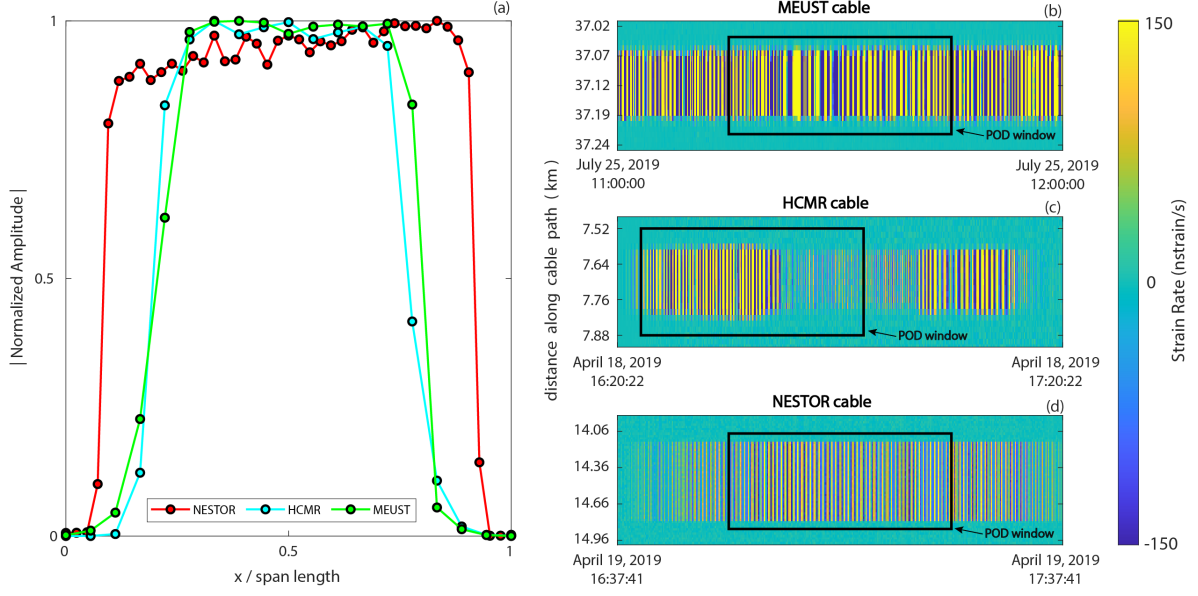
Figure 7. Dominant normal mode of Low-Frequency oscillations recorded by DAS. (a) Proper Orthogonal fundamental Modes of the NESTOR (red), HCMR (cyan) and MEUST (green) cables, extracted through POD of LF oscillations. (b, c and d) 1-hr-long windows of low-pass filtered strain rate featuring LF oscillations along the MEUST, HCMR and NESTOR cable, respectively. Strain rate is filtered below 2 Hz. (black rectangles) 30-min-long windows of strain rate along cable spans of 180.00, 345.60 and 806.40 m selected in the MEUST, HCMR and NESTOR cable, respectively, for POD calculations. The dominant normal mode obtained from the three cables exhibits a quasi-uniform strain rate along the cable span featuring the oscillation, similar to a box-car shape.

by beam theory deformation under VIV. Bourguet and Triantafyllou (2015) reported box-car shaped root-mean-square (RMS) displacements in numerical simulations of VIV along a flexible cylinder fixed at both ends. However, a box-shaped RMS displacement does not imply a box-shaped strain rate. More useful insight is derived here from beam theory. According to classical beam theory, the longitudinal strain $\varepsilon_{(x)}$ of a long and slender beam - a component designed to support transverse load by bending only - laying on two supports, is proportional to its deflection $y(x)$ through its curvature κ: $\varepsilon_{(x)} = -\kappa \, y(x)$, with $\kappa = \frac{y''(x)}{(1+y'(x)^2)^{3/2}}$ (Timoshenko and Goodier 1970; Kelly 2013). Assuming that the slope of the deflection curve is small $(y'(x) << 1)$, which is expected for small deformations of fibre cables, leads to $\kappa \approx y''(x)$, and the longitudinal strain of the beam becomes proportional to its bending as (Kelly 2013):

$$\varepsilon_{(x)} \approx -y''(x) \, y(x) \tag{3}$$

We considered the fibre segments featuring LF oscillations as beams that bend due to the transverse oscillating load induced by the drag forces during VIV. Moreover, we assumed that

the tensioned fibres have mode-shapes given by a sine function $y(x) = A\sin(n\pi x/L)$, with L the cable span length and A an unknown amplitude, as suggested by Lie and Kaasen (2006) for a riser manifesting VIV due to a linearly sheared flow. Under those assumptions, equation (3) shows that the dominant normal modes for longitudinal strain should have a sine-square shape (*Supplementary Figure 9*). Equation (3) explains well the zero strain at both ends of the dominant normal modes, and the absence of strain nodes within the oscillating span, two features that cannot be explained by the vibrating string theory. However, it predicts a maximum of strain at the mid-span, which is different from the quasi-uniform strain of the observed dominant normal mode. More investigation is needed to completely elucidate what physical process controls the shape of the dominant normal mode extracted from DAS-recorded LF oscillations.

Evidence suggests that the HF and LF oscillations presented here are associated with different conditions of the mechanical cable/seafloor coupling. These two types of oscillations have different frequency content and normal mode shapes. Besides, LF oscillations have been associated with deep ocean currents hitting suspended fibre cable spans, which generate vortex-induced vibrations (Mata Flores et al. 2022). The ocean-driven origin of the LF oscillations contrasts with the earthquake-triggered HF oscillations presented in this study. We calculate cross-correlation traces from cable segments featuring LF oscillations. To prevent high-frequency noise, the strain rate data were first low-pass filtered at 2 Hz. Then, cross-correlations were computed over 30-min-long windows, using as reference trace the first oceanward DAS channel featuring the oscillations. The cross-correlation traces do not show cable waves (*Supplementary Figure 6*), thus LF oscillations cannot be used to identify fibre cable spans pinned between two points along the seafloor. Further work is warranted to locate suspended sections of seafloor fiber cables with precision, by combining the detection of the LF oscillations we present here with a detailed bathymetry model along the fibre cable path. We suspect that the assessment of fibre cable spans likely to suffer damage due to overload could be performed through the detection of LF fibre cable oscillations.

5   DISCUSSION

Our results suggest that LF and HF oscillations can be detected on seafloor fibre optic cables regardless of the geographic location and the interrogator used for the DAS acquisition. The data analyzed here was recorded on three underwater fibre cables deployed in two different locations of the Mediterranean sea. The datasets were acquired by DAS interrogators that use distinct optical measurement principles. Yet, HF oscillations were observed in all cases.

Similarly, LF oscillations were recorded along both the Toulon and Methoni cables. We expect the two vibration regimes can be detected in any seafloor fibre cable interrogated by DAS, since they are generated by mechanisms that are independent of the optical properties of DAS.

LF and HF oscillations result from independent mechanisms. We showed here that HF oscillations are triggered by seismic waves from earthquakes, while Mata Flores et al. (2022) showed that LF oscillations are driven by ocean currents. We found here that the frequency content of LF and HF oscillations is well separated and their occurrence is not correlated, which suggests distinct sources for each vibration regime. The frequencies of HF oscillations depend on span length (Figure 3) and, for the three steel-armoured fiber cables used in this study, are higher than 2 Hz and lower than 18 Hz, along span lengths ranging from 115.20 to 748.80 m. On the other hand, the frequency content of LF oscillations observed in this study rarely exceeds 1 Hz nor depends on span length. LF and HF oscillations can be recorded simultaneously, as shown in Fig. 2.c, without their characteristics being affected, which suggests the two vibration regimes are not mutually exclusive. Nevertheless, further work should be aimed to determine if HF oscillations occur on longer cable spans than those found here, at frequencies that overlap with LF oscillations.

We propose that LF and HF oscillations can be used to assess the mechanical coupling between offshore fibre cables and the seafloor. LF oscillations require hanging cable segments, as documented by Mata Flores et al. (2022). We interpret here that HF oscillations require two pinning points that prevent longitudinal motion of the cable and trap compressional cable waves along a finite span length. The identification of fibre cable segments featuring LF or HF oscillations can supply information of the mechanical cable/seafloor coupling without deploying additional instruments or resources. We propose to use the detection of LF and HF oscillations to monitor the spatial distribution of the mechanical coupling between offshore fibre cables and the sea bottom. Tracking the amplitude of strain rate via its standard deviation in the LF band is a convenient approach to identify cable sections that are presumably hanging and thus might suffer damage due to overload or fatigue, as shown in Fig. 8 for the NESTOR and HCMR cables. The identification of HF oscillations can pinpoint the cable segments that are least appropriate for seismological purposes due to high noise made of trapped cable waves. On the other hand, the temporal evolution of the mechanical cable/seafloor coupling may also be tracked through the detection of LF oscillations. Submarine slopes starting at the edge of continental shelves are usually eroded into deep canyons and other small channels that accumulate sediments, until they become unstable and initiate
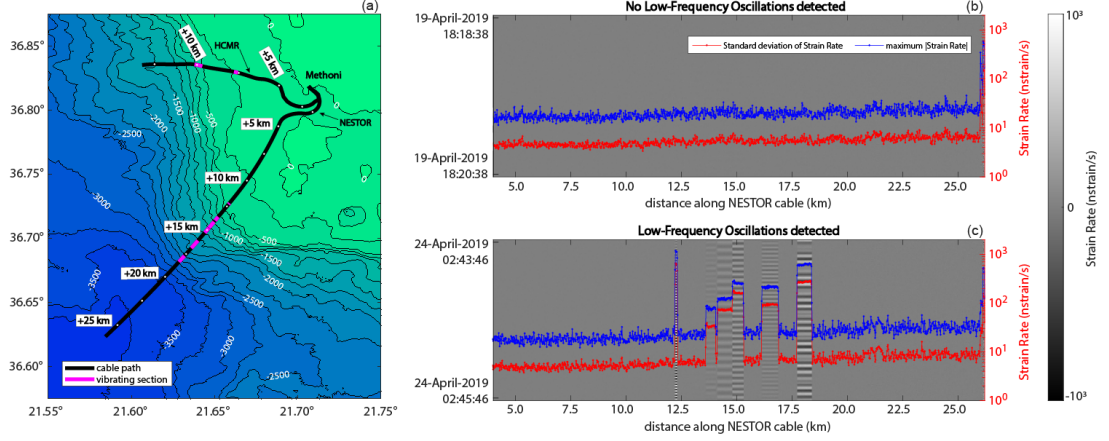
Figure 8. Fibre segments of the NESTOR and HCMR cables presumably vibrating are highlighted by Low-Frequency Oscillations. (a) NESTOR and HCMR cable trajectories offshore Methoni Bay, Greece (black), and location of the detected vibrating sections (magenta). Positive and negative values indicate the distance along the cable path in kilometers and the seafloor depth in meters, respectively. (b) Low-pass filtered strain rate along NESTOR cable between km 5 and 26, from 19-April-2019 18:18:38 to 18:20:38 UTC (black and white), compared with the variation across the cable of the maximum positive strain rate (blue) and the standard deviation of the strain rate (red). Strain rate is low-pass filtered below 2 Hz. (c) Same as b, but from 24-April-2019 02:43:46 to 02:45:46 UTC. Throughout the continental slope between km 10 and 20 across the NESTOR fibre in (c), where suspended portions of the fibre cable are expected, 6 segments featuring quasi-uniform strain rate correlate with an increase of the maximum positive strain rate and the standard deviation of the strain rate.

erosion by sedimentary mass flows such as turbidity currents (Shepard 1981; Mitchell 2005). In submarine canyons, erosion may alternate locally with sediment deposition (Menard 1961), which exposes underwater fibre cables traversing continental slopes to different rates of sediment accumulation. Most of the suspended sections we identified in this study are located along cable segments that cross continental slopes, as shown in Fig. 8 for the cables in the Methoni bay. Hence, sediment deposition may progressively bury hanging sections until LF oscillations are no longer detectable. We suggest to conduct longer DAS-experiments in fibre cables traversing continental slopes, preferably in areas with high erosion/deposition rates, to verify the relation between sedimentation and the vanishing of LF oscillations in time.

6 CONCLUSIONS

We identified and characterised two vibration regimes of underwater fibre optic cables recorded by DAS along three cables situated in the Mediterranean sea. We observed that seismic

waves excite high-frequency oscillations, with fundamental frequencies > 2 Hz, composed of longitudinal waves that remain trapped along cable segments presumably pinned between two points in the seafloor. The frequency vs length relation and normal mode shapes extracted from high-frequency oscillations are consistent with 1D wave propagation in a structure with fixed ends. Cross-correlation shows that these waves travel along the cable structure with a speed ranging from 3939 to 4080 m/s, close to that of longitudinal waves propagating along the steel armouring of the cables. We have also identified fibre cable segments featuring low-frequency oscillations, with fundamental frequencies < 1 Hz, which have been previously associated to vortex-induced vibration of suspended cable sections caused by deep sea currents. We further showed that these low-frequency oscillations feature quasi-uniform strain rates along each vibrating section.

This is the first study, to our knowledge, assessing the mechanical coupling between offshore fibre cables and the seafloor based on the detection of high-frequency cable waves and low-frequency vortex induced vibrations. We propose to use the detection of high-frequency and low-frequency oscillations to monitor the spatio-temporal evolution of the mechanical coupling between fibre cables and the seafloor. The former may help to identify the most appropriate cable segments for seismology purposes, and the latter may supply a non-invasive method to monitor cable sections likely to suffer damage due to overload or fatigue.

DATA AVAILABILITY

The DAS-strain rate recordings used to generate figures 2-8 are available in the following OSF repository: https://osf.io/srv76/.

REFERENCES

G. Aggouras, E. Anassontzis, A. Ball, G. Bourlis, W. Chinowsky, E. Fahrun, G. Grammatikakis, C. Green, P. Grieder, P. Katrivanos, et al. A measurement of the cosmic-ray muon flux with a module of the nestor neutrino telescope. *Astroparticle Physics*, 23(4):377–392, 2005.

E. Anassontzis and P. Koske. Deep-sea station connected by cable to shore. *Sea Technology*, 44(7): 10–14, 2003.

E. Anassontzis, M. Barone, E. Fahrun, C. Foudas, G. Gialas, G. Grammatikakis, S. Katsanevas, C. Kourkoumelis, A. Manousakis-Katsikakis, A. Odian, et al. Status of nestor, a deep sea neutrino telescope in the mediterranean. *Nuclear Physics B-Proceedings Supplements*, 66(1-3):247–251, 1998.

R. Bourguet and M. S. Triantafyllou. Vortex-induced vibrations of a flexible cylinder at large inclination angle. 373(2033):20140108, 2015. ISSN 1364-503X, 1471-2962. doi: 10.1098/rsta.2014.0108. URL https://royalsocietypublishing.org/doi/10.1098/rsta.2014.0108.

H. Chang and N. Nakata. Investigation of time-lapse changes with das borehole data at the brady geothermal field using deconvolution interferometry. *Remote Sensing*, 14(1):185, 2022.

N. Collaboration, E. Anassontzis, M. Barone, G. Contopoulos, G. Fanourakis, G. Grammatikakis, P. Hatzios, P. Ioannou, G. Kalkanis, S. Katsanevas, et al. Nestor: A neutrino particle astrophysics underwater laboratory for the mediterranean. *Nuclear Physics B-Proceedings Supplements*, 35:294–300, 1994.

P. Coyle. KM3NeT-ORCA: Oscillation Research with Cosmics in the Abyss. 888: 012024, 2017. ISSN 1742-6588, 1742-6596. doi: 10.1088/1742-6596/888/1/012024. URL https://iopscience.iop.org/article/10.1088/1742-6596/888/1/012024.

J. Cusumano and B.-Y. Bai. Period-infinity periodic motions, chaos, and spatial coherence in a 10 degree of freedom impact oscillator. *Chaos, Solitons & Fractals*, 3(5):515–535, 1993.

J. Cusumano, M. Sharkady, and B. Kimble. Spatial coherence measurements of a chaotic flexible-beam impact oscillator. In *Proceedings of the 1993 ASME Winter Annual Meeting*, pages 13–22. Publ by ASME, 1993.

B. Feeny. On proper orthogonal co-ordinates as indicators of modal activity. *Journal of Sound and Vibration*, 255(5):805–817, 2002.

B. Feeny and R. Kappagantu. On the physical interpretation of proper orthogonal modes in vibrations. *Journal of sound and vibration*, 211(4):607–616, 1998.

M. R. Fernández-Ruiz, E. L. Williams, R. Magalhaes, R. Vanthillo, L. Costa, Z. Zhan, S. Martin-Lopez, M. Gonzalez-Herraez, and H. F. Martins. Teleseisms monitoring using chirped-pulse φotdr. In *Seventh European Workshop on Optical Fibre Sensors*, volume 11199, page 1119921. International Society for Optics and Photonics, 2019.

A. H. Hartog. *An introduction to distributed optical fibre sensors*. CRC press, 2017.

W. Haynes. edition 95. crc handbook of chemistry and physics, 2014.

R. Kappagantu and B. Feeny. An" optimal" modal reduction of a system with frictional excitation.

Journal of Sound and vibration, 224(5):863–877, 1999.

R. Kappagantu and B. Feeny. Part 2: Proper orthogonal modal modeling of a frictionally excited beam. *Nonlinear Dynamics*, 23(1):1–11, 2000.

P. Kelly. Solid mechanics part i: An introduction to solid mechanics. solid mechanics lecture notes, 2013.

P. Lamare. The meust deep sea infrastructure in the toulon site. 116: 09001, 2016. ISSN 2100-014X. doi: 10.1051/epjconf/201611609001. URL http://www.epj-conferences.org/10.1051/epjconf/201611609001.

H. Lie and K. Kaasen. Modal analysis of measurements from a large-scale viv model test of a riser in linearly sheared flow. *Journal of fluids and structures*, 22(4):557–575, 2006.

N. J. Lindsey, E. R. Martin, D. S. Dreger, B. Freifeld, S. Cole, S. R. James, B. L. Biondi, and J. B. Ajo-Franklin. Fiber-optic network observations of earthquake wavefields. *Geophysical Research Letters*, 44(23):11–792, 2017.

N. J. Lindsey, T. C. Dawe, and J. B. Ajo-Franklin. Illuminating seafloor faults and ocean dynamics with dark fiber distributed acoustic sensing. *Science*, 366(6469):1103–1107, 2019.

I. Lior, A. Sladen, D. Rivet, J. Ampuero, Y. Hello, C. Becerril, H. F. Martins, P. Lamare, C. Jestin, S. Tsagkli, and C. Markou. On the Detection Capabilities of Underwater Distributed Acoustic Sensing. 126(3), 2021. ISSN 2169-9313, 2169-9356. doi: 10.1029/2020JB020925. URL https://onlinelibrary.wiley.com/doi/10.1029/2020JB020925.

E. R. Martin, F. Huot, Y. Ma, R. Cieplicki, S. Cole, M. Karrenbach, and B. L. Biondi. A seismic shift in scalable acquisition demands new processing: Fiber-optic seismic signal retrieval in urban areas with unsupervised learning for coherent noise removal. *IEEE Signal Processing Magazine*, 35 (2):31–40, 2018.

D. Mata Flores, A. Sladen, J.-P. Ampuero, E. D. Mercerat, and D. Rivet. Monitoring deep sea currents with seafloor distributed acoustic sensing. 2022.

A. Mateeva, J. Lopez, H. Potters, J. Mestayer, B. Cox, D. Kiyashchenko, P. Wills, S. Grandi, K. Hornman, B. Kuvshinov, et al. Distributed acoustic sensing for reservoir monitoring with vertical seismic profiling. *Geophysical Prospecting*, 62(4-Vertical Seismic Profiling and Microseismicity Frontiers): 679–692, 2014.

H. Menard. Some rates of regional erosion. *The Journal of geology*, 69(2):154–161, 1961.

D. E. Miller, X. Zeng, J. R. Patterson, E. C. Reinisch, H. Wang, and M. Robertson. Das and dts at brady hot springs : Observations about coupling and coupled interpretations. 2018.

N. C. Mitchell. Interpreting long-profiles of canyons in the usa atlantic continental slope. *Marine Geology*, 214(1-3):75–99, 2005.

J. D. Munn, T. I. Coleman, B. L. Parker, M. J. Mondanos, and A. Chalari. Novel cable coupling technique for improved shallow distributed acoustic sensor vsps. *Journal of Applied Geophysics*, 138:72–79, 2017. ISSN 0926-9851. doi: https://doi.org/10.1016/j.jappgeo.2017.01.007. URL

https://www.sciencedirect.com/science/article/pii/S0926985117300228.

J. Pastor-Graells, H. F. Martins, A. Garcia-Ruiz, S. Martin-Lopez, and M. Gonzalez-Herraez. Single-shot distributed temperature and strain tracking using direct detection phase-sensitive otdr with chirped pulses. *Optics express*, 24(12):13121–13133, 2016.

M. R. Fernández-Ruiz, L. Costa, and H. F. Martins. Distributed acoustic sensing using chirped-pulse phase-sensitive otdr technology. *Sensors*, 19(20):4368, 2019.

F. P. Shepard. Submarine canyons: multiple causes and long-time persistence. *AAPG bulletin*, 65(6): 1062–1077, 1981.

A. Sladen, D. Rivet, J. P. Ampuero, L. De Barros, Y. Hello, G. Calbris, and P. Lamare. Distributed sensing of earthquakes and ocean-solid earth interactions on seafloor telecom cables. *Nature communications*, 10(1):1–8, 2019.

R. Thompson, G. Alers, D. Thompson, and M. Tennison. Dispersion of flexural elastic waves in honeycomb sandwich panels. *The Journal of the Acoustical Society of America*, 57(5):1119–1127, 1975.

S. P. Timoshenko and J. Goodier. ¹heory of elasticity. *McGraw-Hill International Editions: New York*, 341:342, 1970.

E. F. Williams, M. R. Fernández-Ruiz, R. Magalhaes, R. Vanthillo, Z. Zhan, M. González-Herráez, and H. F. Martins. Distributed sensing of microseisms and teleseisms with submarine dark fibers. 10(1):5778, 2019. ISSN 2041-1723. doi: 10.1038/s41467-019-13262-7. URL http://www.nature.com/articles/s41467-019-13262-7.

A. Yigit and S. Choura. Vibration confinement in flexible structures via alteration of mode shapes by using feedback. *Journal of Sound and Vibration*, 179(4):553–567, 1995.

Z. Zhan. Distributed acoustic sensing turns fiber-optic cables into sensitive seismic antennas. *Seismological Research Letters*, 91(1):1–15, 2020.

Supplementary Material for "*Identification of two vibration regimes of underwater fibre optic cables by Distributed Acoustic Sensing*"

D. Mata Flores[1] , J.-P. Ampuero[1] , E. D. Mercerat[2] , D. Rivet[1] , A. Sladen[1]

[1] Université Cote d'Azur, CNRS, Observatoire de la Cote d'Azur, IRD, Géoazur, Sophia Antipolis, 250 rue Albert Einstein, 06560, Valbonne, France.

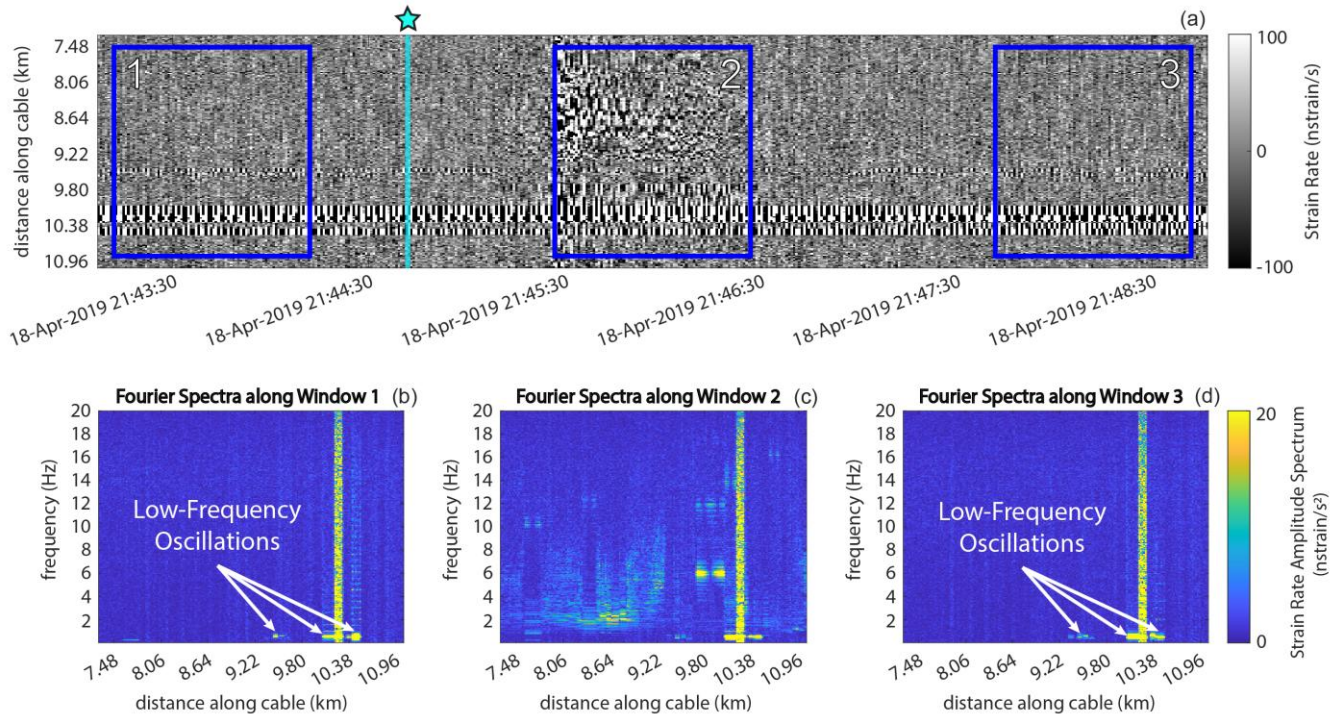[2] CEREMA, Méditerranée, 500 Rte des Lucioles, 06560, Valbonne, France.

Contents of this file

Introduction

This supplementary contains additional figures and calculations.

**Supplementary Figure 1. High-frequency vibrations triggered along the HCMR fibre cable after a M$_L$-3.7 earthquake is recorded by DAS.** (a) Low-pass filtered strain rate between km 7.48 and 10.96 along the HCMR cable, from 18-April-2019 21:43:07 to 21:48:47 UTC. Strain rate is filtered below 20 Hz. (cyan star) Origin time of the M$_L$-3.7 earthquake of Fig. 1 is indicated as reference. Waves trapped along certain cable sections can be observed in Window 2, after the arrival of seismic waves. (b), (c) and (d) Fourier Spectra between km 7.48 and 10.96 of a 1-min-long window starting: 90 s before the earthquake (1), 40 s after the earthquake (2) and 180 s after the earthquake (3), respectively. Fourier spectra before (b) and after (d) the earthquake are dominated by excited frequencies lower than 1 Hz. Fundamental-and-harmonic frequencies higher than 2 Hz appear after the arrival of seismic waves along different cable spans (c), from km 7.48 to 10.20.
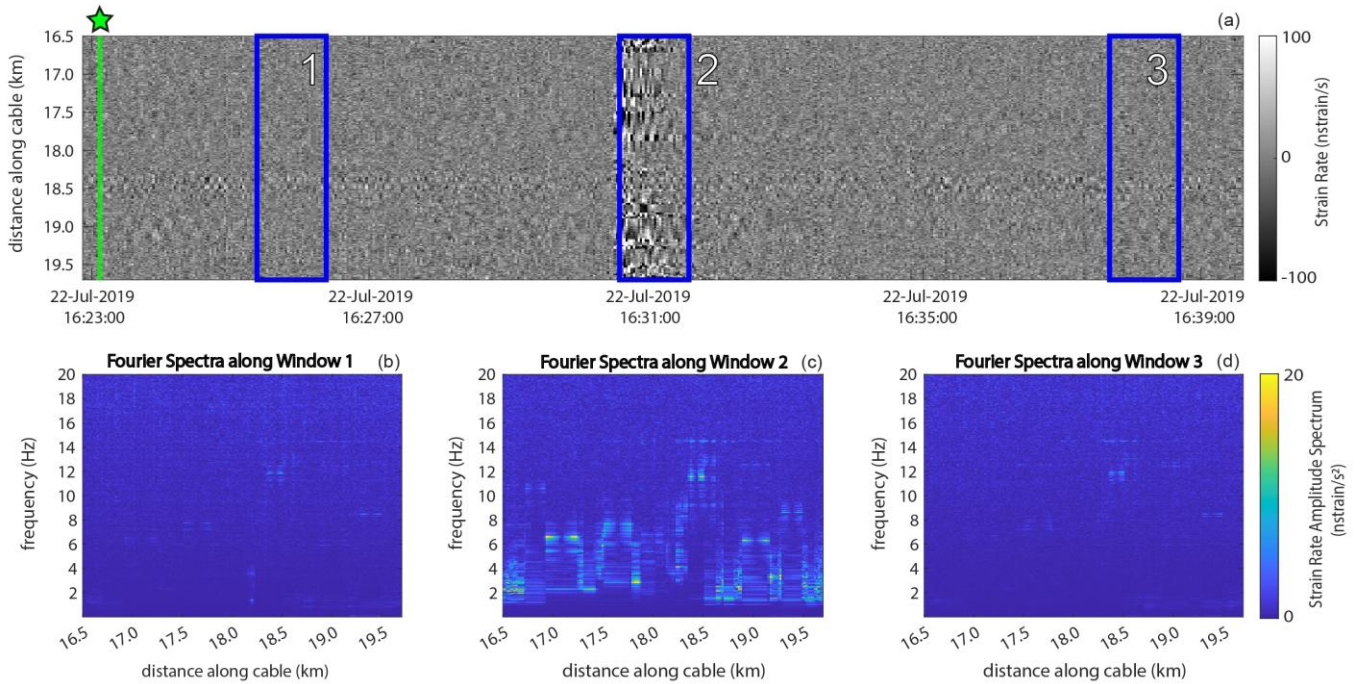
Supplementary Figure 2. High-frequency vibrations triggered along the MEUST fibre cable after a M_L-3.9 earthquake is recorded by DAS. (a) Low-pass filtered strain rate between km 16.50 and 19.70 along the MEUST cable, from 22-July-2019 16:23:00 to 16:39:00 UTC. Strain rate is filtered below 20 Hz. (green star) Origin time of the M_L-3.9 earthquake of Fig. 1 is indicated as reference. Waves trapped along certain cable sections can be observed in Window 2, after the arrival of seismic waves. (b), (c) and (d) Fourier Spectra between km 16.50 and 19.70 of a 1-min-long window starting: 2 min and 16 s after the earthquake (1), 7min and 29 s after the earthquake (2) and 14 min and 34 s after the earthquake (3), respectively. No significant signals are appreciated in Fourier spectra (b) and (d). Fundamental frequencies higher than 2 Hz appear after the arrival of seismic waves along different cable spans (c), from km 16.50 to 19.70.
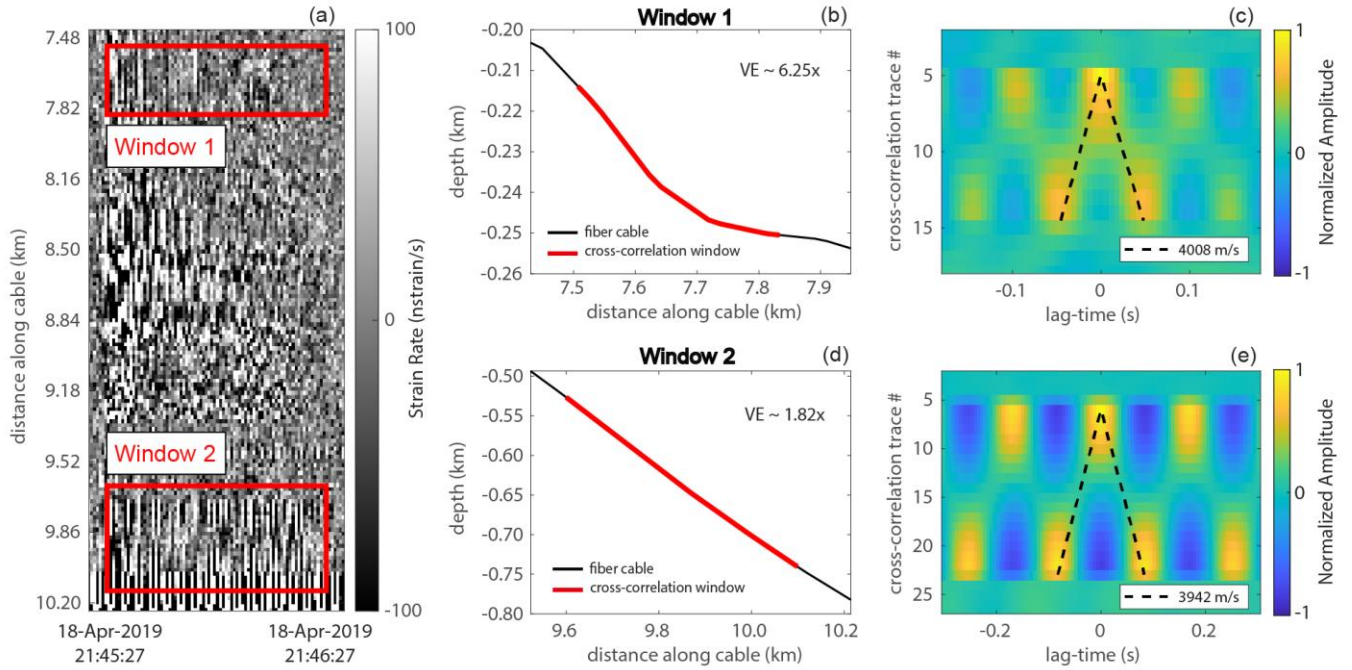
Supplementary Figure 3. Longitudinal trapped waves detected by DAS along cable segments of the HCMR cable featuring earthquake-triggered vibrations. (a) Low-pass filtered strain rate between km 7.48 and 10.20 along the HCMR cable, from 18-April-2019 21:45:27 to 21:46:27 UTC. Strain rate is filtered below 20 Hz. (red rectangles) Two 60-s-long windows of 172.80 (1) and 345.60 m (2) width are indicated as reference. (b) Bathymetry profile between km 7.45 and 7.95 along the cable path (VE stands for Vertical Exaggeration). The red line highlights the location of window 1 in (a). (c) Cross-correlation traces calculated over window 1 in (a), and relative to the trace reference number 5, km 7.60 along the cable. Amplitudes are normalized by the maximum of the cross-correlation traces. A longitudinal trapped wave bouncing forward and backward along the cable span with a speed of 4008 m/s can be clearly observed (black dashed lines). (d and e) Same as b, and c, but for a cable section traversing the continental slope between km 9.5 and 10.2, window 2 in (a).
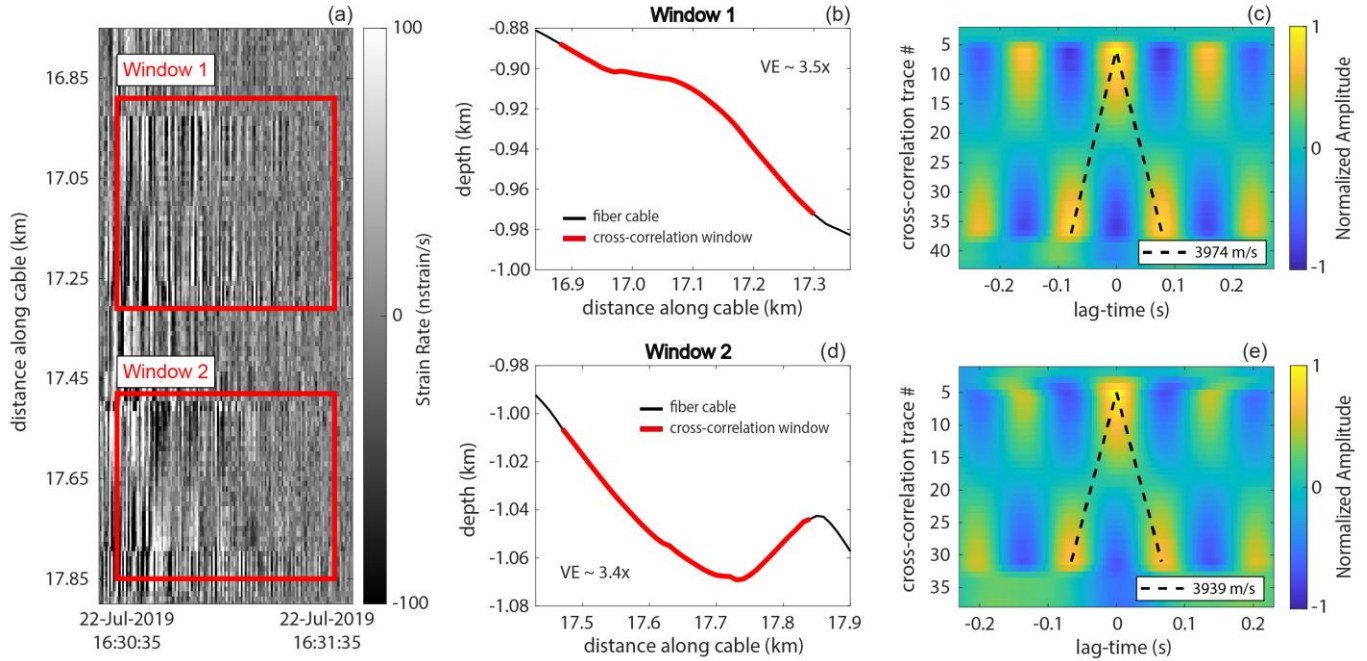
**Supplementary Figure 4. Longitudinal trapped waves detected by DAS along cable segments of the MEUST cable featuring earthquake-triggered vibrations.** (a) Low-pass filtered strain rate between km 16.75 and 17.90 along the MEUST cable, from 22-July-2019 16:30:35 to 16:31:35 UTC. Strain rate is filtered below 20 Hz. (red rectangles) Two 60-s-long windows of 420 (1) and 370 m (2) width are indicated as reference. (b) Bathymetry profile between km 16.84 and 17.36 along the cable path (VE stands for Vertical Exaggeration). The red line highlights the location of window 1 in (a). (c) Cross-correlation traces calculated over window 1 in (a), and relative to the trace reference number 5, km 16.94 along the cable. Amplitudes are normalized by the maximum of the cross-correlation traces. A longitudinal trapped wave bouncing forward and backward along the cable span with a speed of 3974 m/s can be clearly observed (black dashed lines). (d and e) Same as b, and c, but for a cable section presumably suspended between km 17.43 and 17.90, window 2 in (a).
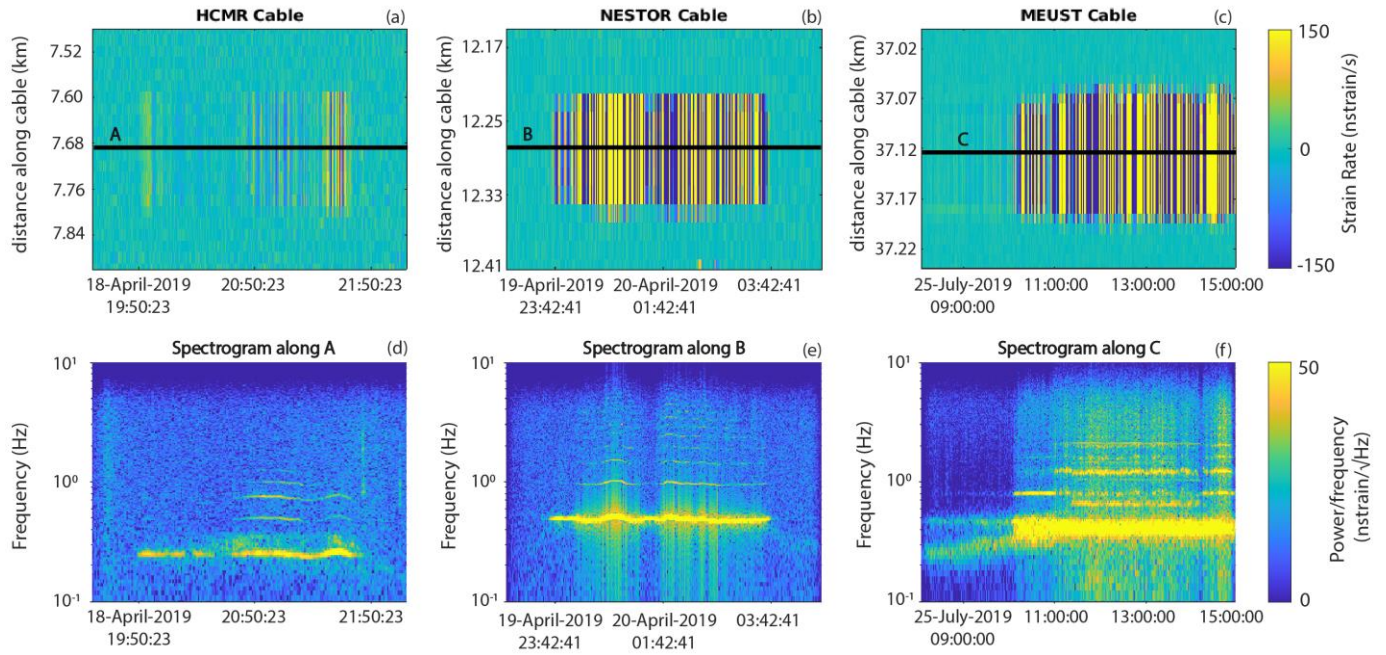
Supplementary Figure 5. Harmonics of Vortex-Induced Vibrations (VIV) recorded by DAS along suspended sections of submarine fibre cables. Low-pass filtered strain rate between km 7.52 and 7.84 from 18-April-2019 19:20:23 to 22:20:23 UTC along the HCMR cable (a), between km 12.17 and 12.41 from 19-April-2019 22:42:41 to 20-April 04:42:41 UTC along the NESTOR cable (b), and between km 37.02 and 37.22 from 25-July-2019 08:30:00 to 15:00:00 along the MEUST cable (c). DAS-strain rate data are filtered below 5 Hz. Black lines indicate the center of the cable segment featuring Low-Frequency (LF) oscillations. (d, e, f) Spectrograms of strain rate at A, B and C, respectively. Higher harmonic frequencies of VIV are excited along cable segments displaying LF oscillations.
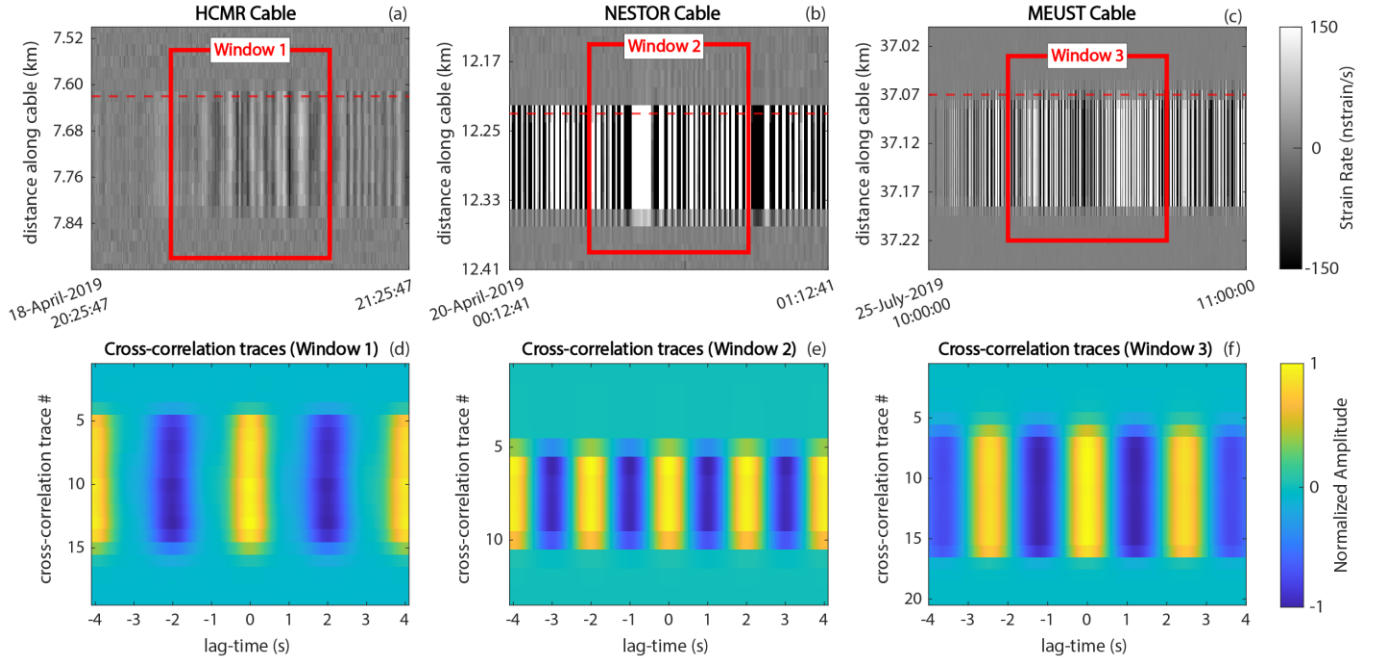
Supplementary Figure 6. Cross-correlation analysis of underwater fibre cables displaying Low-Frequency oscillations. Low-pass filtered strain rate between km 7.52 and 7.90 from 18-April-2019 20:25:47 to 21:25:47 UTC along the HCMR cable (a), between km 12.17 and 12.41 from 20-April-2019 00:12:41 to 01:12:41 UTC along the NESTOR cable (b), and between km 37.02 and 37.22 from 25-July-2019 10:00:00 to 11:00:00 along the MEUST cable (c). DAS-strain rate data are filtered below 2 Hz. (red rectangles) 30-min-long windows of strain rate of 345.60 (window 1), 230.40 (window 2) and 190 (window 3) m width for the HCMR, NESTOR and MEUST cable, respectively. (d, e and f) Cross-correlation traces calculated over window 1, 2 and 3 respectively. Dashed red lines in a, b and c indicate the reference traces used for cross-correlation. Amplitudes are normalized by the maximum of the cross-correlation traces. The cross-correlation of cable segments featuring Low-Frequency oscillations does not reveal cable waves.
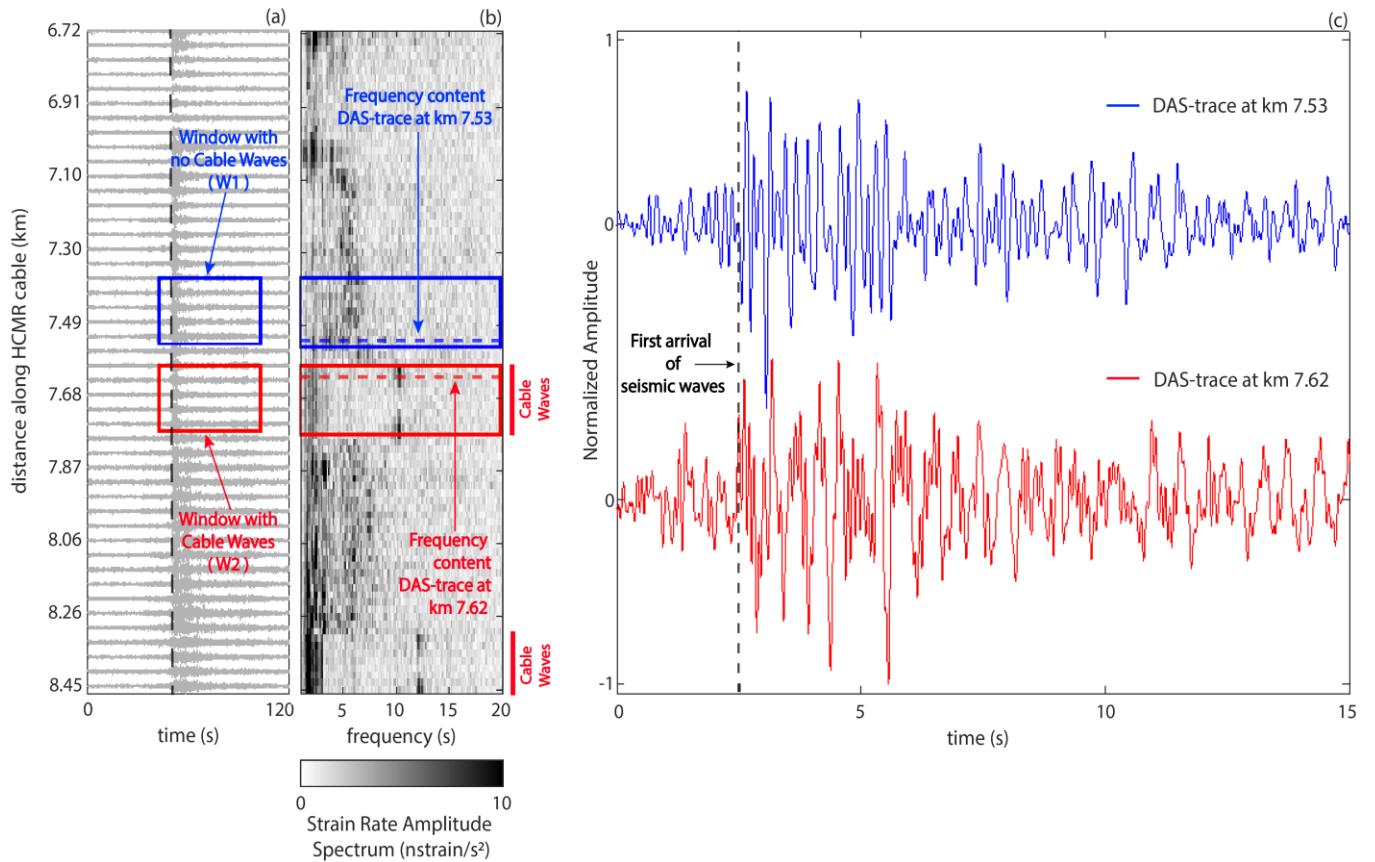
Supplementary Figure 7. Noise generated by cable waves in DAS-strain rate recordings of the HCMR cable. (a) 120-s-long traces of band-pass filtered strain rate between km 6.72 and 8.45 of the HCMR cable. Traces are filtered between 1 and 12 Hz and are represented each 38.4 m. (dashed line) Arrival of seismic waves due to the M_L-3.7 earthquake of Fig. 1. (blue and red rectangles) As reference, 60-s-long windows of 172.80 m width indicate whether cable waves are absent (W1) or detected (W2), respectively. (b) Fourier spectra between km 6.72 and 8.45 of a 60-s-long window starting at the same time of W1. (red and blue rectangles) Frequency content of W1 and W2, respectively. (c) 15-s-long traces of strain rate along: km 7.53 in W1 (blue), and km 7.62 in W2 (red). Amplitudes are normalized by the maximum strain rate of each channel. Cable waves are clearly recorded in W2, which may explain the high monochromatic noise that dominates the signal along the DAS-trace in km 7.62, after the arrival of seismic waves, compared to the DAS-trace in km 7.53.
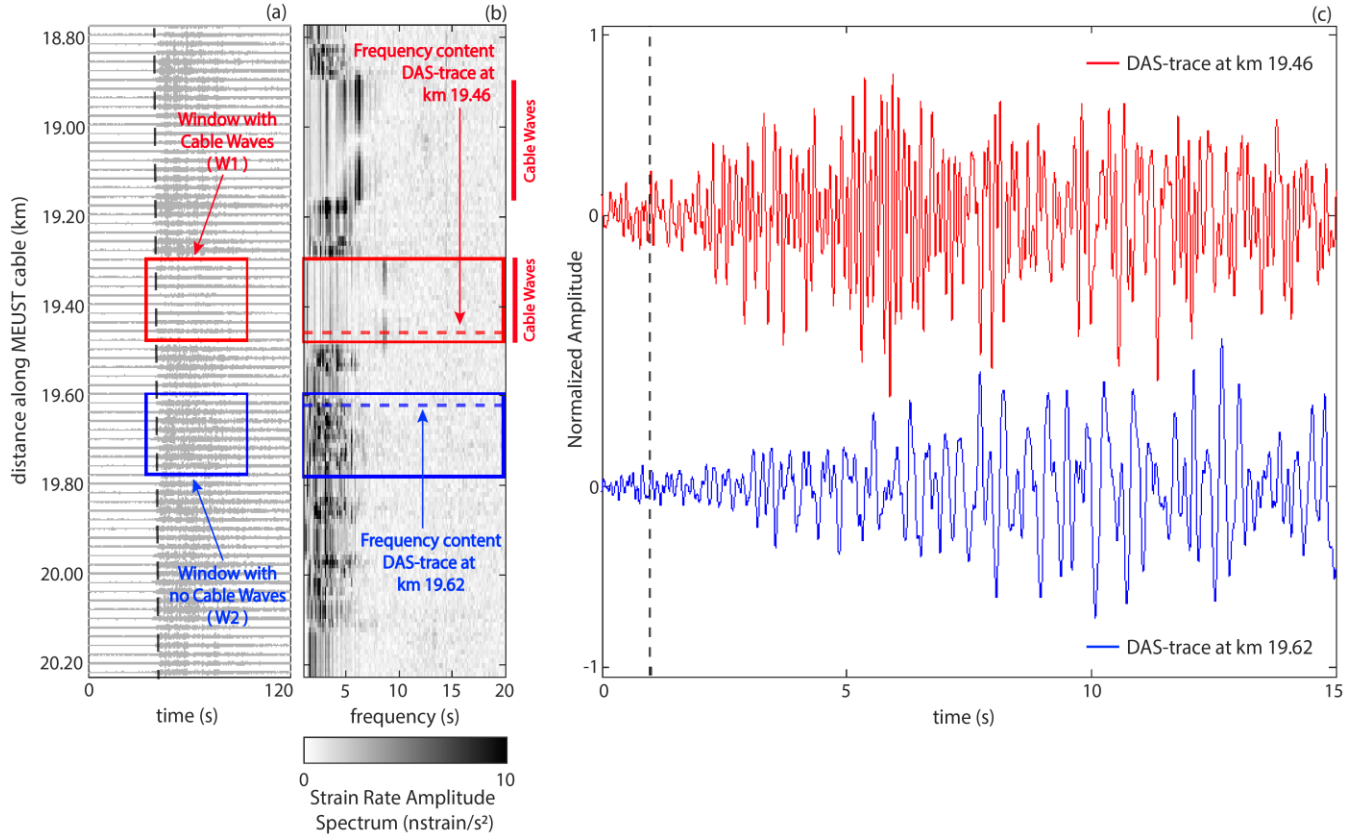
Supplementary Figure 8. Noise generated by cable waves in DAS-strain rate recordings of the MEUST cable. (a) 120-s-long traces of band-pass filtered strain rate between km 18.80 and 20.20 of the MEUST cable. Traces are filtered between 1 and 12 Hz and are represented each 20 m. (dashed line) Arrival of seismic waves due to the M_L-3.9 earthquake of Fig. 1. (red and blue rectangles) As reference, 60-s-long windows of 180 m width indicate whether cable waves are detected (W1) or absent (W2), respectively. (b) Fourier spectra between km 18.80 and 20.20 of a 60-s-long window starting at the same time of W1. (red and blue rectangles) Frequency content of W1 and W2, respectively. (c) 15-s-long traces of strain rate along: km 19.46 in W1 (red), and km 19.62 in W2 (blue). Amplitudes are normalized by the maximum strain rate of each channel. Cable waves are clearly recorded in W1, which may explain the high monochromatic noise that dominates the signal along the DAS-trace in km 19.46, after the arrival of seismic waves, compared to the DAS-trace in km 19.62.
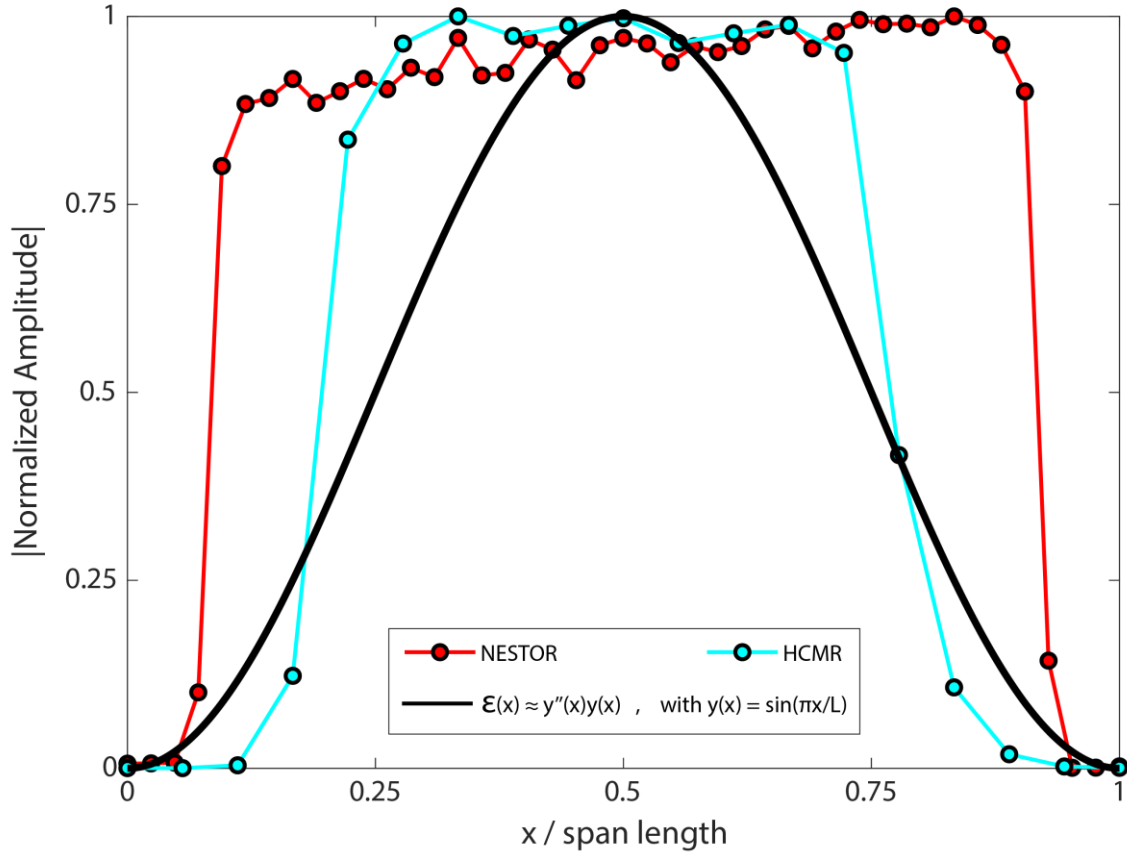
Supplementary Figure 9. Normal modes of Low-Frequency (LF) oscillations compared to longitudinal strain predicted by the beam theory. (red and cyan) Dominant normal modes of LF oscillations recorded by DAS along the NESTOR and HCMR cable, respectively. (black) Longitudinal strain ($\varepsilon_{(x)}$) of a long and slender beam predicted by Timoshenko's beam theory as a function of the beam's deflection ($y_{(x)}$) and bending ($y''_{(x)}$). It is assumed that fibres have mode-shapes given by a sine function: $y_{(x)}$ = $\sin(\pi x/L)$. Amplitudes in the vertical and horizontal axis are normalized by the maximum strain rate and the cable span length (L), respectively. The relation $\varepsilon_{(x)} = y''_{(x)} y_{(x)}$ explains well the zero strain at both ends of the dominant normal modes, and the absence of strain nodes within the vibrating span. However, it predicts a maximum of strain at the mid-span, which is different from the quasi-uniform strain of the observed dominant normal modes.

Proper Orthogonal Decomposition based on DAS-recorded time series of strain rate.

According to Feeny (2002), Proper Orthogonal Decomposition (POD) is a statistical method that is used to find optimal distributions of energy from a set of time series. POD is commonly applied to a dataset of dynamical quantities recorded at M locations (Feeny, 2002). Here, M stands for the number of channels along the fibre cable that record DAS-strain rate (x) from a time t_1 to t_N, such as $x_i = (x_i(t_1), x_i(t_2), \ldots, x_i(t_N))^T$, for i = 1, 2, . . . , M. Prior to POD calculations, time series of DAS-strain rate are used to generate a $N \times M$ matrix, as follows (Feeny, 2002):

$$\mathbf{X} = [\, x_1, x_2, \ldots, x_M \,]$$

Then, a $M \times M$ correlation matrix $\mathbf{R} = (1/N)\mathbf{X}^T\mathbf{X}$ is formed, from which eigenvectors ($\mathbf{v}$) and eigenvalues ($\boldsymbol{\lambda}$) are extracted. The correlation matrix $\mathbf{R}$ is real and symmetric, which guarantees that $\mathbf{v}$ and $\boldsymbol{\lambda}$ are orthogonal (Feeny, 2002). Moreover, $\mathbf{v}$ contains the proper orthogonal modes (POMs) and $\boldsymbol{\lambda}$ the proper orthogonal values (POVs) of $\mathbf{R}$, respectively, i.e. the principal axes of inertia of the DAS-data and the signal power of each corresponding POM (Feeny and Kappagantu, 1998; Lumley, 1967; Cusumano and Bai, 1993; Cusumano et al., 1993; Berkooz et al., 1993).

POMs can be used as basis functions to decompose the dynamics of the DAS-recordings into modal co-ordinates $\mathbf{q}$(t) (Han and Feeny, 2001). To do so, a proper orthogonal modal matrix $\mathbf{V}$ is defined, as follows (Feeny, 2002):

$$\mathbf{V} = [\, \mathbf{v}_1, \mathbf{v}_2, \ldots, \mathbf{v}_M]$$

Then, modal co-ordinates with elements q_i(t), i = 1, 2, . . . , M are defined, such that (Feeny, 2002):

$$x(\text{t}) = \sum_{i=1}^{M} q_i(t)\mathbf{v}_i = \mathbf{Vq}$$

The proper orthogonal coordinates (POCs) time series $q_i(t)$ can be extracted from (Feeny, 2002):

$$\mathbf{Q} = \mathbf{XV}$$

where,

$$\mathbf{Q} = [\, q_1, q_2, \ldots, q_M \,]$$

Each modal co-ordinate represents the dynamics in the axis of a corresponding POM (Feeny, 2002).

References:

Feeny, B. F. (2002). On proper orthogonal co-ordinates as indicators of modal activity. *Journal of Sound and Vibration*, *255*(5), 805-817.

Feeny, B. F., & Kappagantu, R. (1998). On the physical interpretation of proper orthogonal modes in vibrations. *Journal of sound and vibration*, *211*(4), 607-616.

Lumley, J. L. (1967). The structure of inhomogeneous turbulent flows. *Atmospheric turbulence and radio wave propagation*, 166-178.

Cusumano, J. P., & Bai, B. Y. (1993). Period-infinity periodic motions, chaos, and spatial coherence in a 10 degree of freedom impact oscillator. *Chaos, Solitons & Fractals*, *3*(5), 515-535.

Cusumano, J. P., Sharkady, M. T & Kimble, B. W. (1993). Spatial coherence measurements of a chaotic flexible-beam impact oscillator. *Aerospace Structures: Nonlinear Dynamics and System Response, American Society of Mechanical Engineers* (33), 13-22.

Berkooz, G., Holmes, P., & Lumley, J. L. (1993). The proper orthogonal decomposition in the analysis of turbulent flows. *Annual review of fluid mechanics*, *25*(1), 539-575.

Han, S., & Feeny, B. F. (2001). Enhanced proper orthogonal decomposition for the modal analysis of homogeneous structures. *Journal of Vibration and Control*, *8*(1), 19-40.